Ocean Modelling 147 (2020) 101569

Contents lists available at ScienceDirect

Ocean Modelling

journal homepage: www.elsevier.com/locate/ocemod

Vertical processes and resolution impact ice shelf basal melting: A multi-model study

David E. Gwyther [a,*], Kazuya Kusahara [b,c], Xylar S. Asay-Davis [d,e], Michael S. Dinniman [f], Benjamin K. Galton-Fenzi [g,b]

[a] Institute for Marine and Antarctic Studies, University of Tasmania, Private Bag 129, Hobart, Tasmania 7001, Australia
[b] Antarctic Climate & Ecosystems Cooperative Research Centre, University of Tasmania, Private Bag 80, Hobart, Tasmania 7001, Australia
[c] Japan Agency for Marine-Earth Science and Technology (JAMSTEC), Yokohama, Kanagawa, Japan
[d] Los Alamos National Laboratory, Los Alamos, NM, USA
[e] Potsdam Institute for Climate Impact Research (PIK), Potsdam, Germany
[f] Center for Coastal Physical Oceanography, Old Dominion University, Norfolk, VA, USA
[g] Australian Antarctic Division, Channel Highway, Kingston, Tasmania, 7050, Australia

ABSTRACT

Understanding ice shelf–ocean interaction is fundamental to projecting the Antarctic ice sheet response to a warming climate. Numerical ice shelf–ocean models are a powerful tool for simulating this interaction, yet are limited by inherent model weaknesses and scarce observations, leading to parameterisations that are unverified and unvalidated below ice shelves. We explore how different models simulate ice shelf–ocean interaction using the 2nd Ice Shelf–Ocean Model Intercomparison Project (ISOMIP+) framework. Vertical discretisation and resolution of the ocean model are shown to have a significant effect on ice shelf basal melt rate, through differences in the distribution of meltwater fluxes and the calculation of thermal driving. Z-coordinate models, which generally have coarser vertical resolution in ice shelf cavities, may simulate higher melt rates compared to terrain-following coordinate models. This is due to the typically higher resolution of the ice–ocean boundary layer region in terrain following models, which allows better representation of a thin meltwater layer, increased stratification, and as a result, better insulation of the ice from water below. We show that a terrain-following model, a z-level coordinate model and a hybrid approach give similar results when the effective vertical resolution adjacent to the ice shelf base is similar, despite each model employing different paradigms for distributing meltwater fluxes and sampling tracers for melting. We provide a benchmark for thermodynamic ice shelf–ocean interaction with different model vertical coordinates and vertical resolutions, and suggest a framework for any future ice shelf–ocean thermodynamic parameterisations.

1. Introduction

Understanding the magnitude and distribution of basal melting beneath ice shelves is critical to assessing current mass loss from Antarctica and projecting the contribution from grounded ice to future sea level rise. Basal melting is the largest source of mass loss (1516 ± 106 Gt yr^{-1}; Liu et al., 2015) from the Antarctic ice sheet, and affects the grounded portions of the ice sheet through the reduction of buttressing of tributary glaciers (Schoof, 2007). Hence, ice loss through basal melting of the floating portions of the ice sheet can lead to glacier acceleration and an increased contribution to sea level. Uncertainty exists in the magnitude of recent Antarctic contribution to global mean sea level rise (Church et al., 2013), with recent estimates of total contribution over the period 1992–2017 being 4.6 ± 1.2 mm (Shepherd et al., 2019) to 7.6 ± 3.9 mm (Shepherd et al., 2018). However, projections of Antarctic contributions under future warming scenarios contain significantly higher uncertainty due to poorly understood processes that might drive rapid ice discharge (e.g. Weertman, 1974; DeConto and Pollard, 2016). In order to reduce uncertainty in current contributions and improve projections of future contributions from Antarctica, we require a better understanding of basal melting.

Numerical models that include the thermodynamic interaction between the ocean and the ice sheet provide the best option for investigating current and future sea level contributions from Antarctica, for example see ROMS: Dinniman et al. (2007); MITgcm: Losch (2008); FESOM: Timmermann et al. (2012); HIM/MOM6: Goldberg et al. (2012a); COCO: Kusahara and Hasumi (2013); FVCOM: Zhou and Hattermann (2020) and NEMO: Mathiot et al. (2017). These models provide wide spatial coverage and fine temporal resolution. Fully coupled ocean–ice sheet models will allow full investigation of how ocean-driven basal melting affects Antarctica, but are as yet still in their infancy for large realistic domains. Ice shelf–ocean models which neglect ice dynamics and assume a steady-state ice geometry are therefore the best current option. These models are based on widely used numerical ocean models, but with modifications to allow for pressure exerted on the water column from the ice, and thermodynamic exchange of heat and freshwater. Ice shelf–ocean models allow this data-poor environment to be explored by simulating both small-scale processes

* Corresponding author.
E-mail address: david.gwyther@gmail.com (D.E. Gwyther).

https://doi.org/10.1016/j.ocemod.2020.101569
Received 20 June 2019; Received in revised form 20 December 2019; Accepted 11 January 2020
Available online 20 January 2020

and the large-scale spatial and temporal evolution of Antarctic basal melting. This is critical to improving estimates of Antarctic mass loss. Furthermore, thermodynamic interaction between ice shelves and the ocean can also modify broad-scale ocean circulation by freshening affecting Antarctic Bottom Water formation and meridional overturning circulation (Jacobs and Giulivi, 2010); and, potentially impact ecosystems by affecting the supply of the micronutrient dissolved iron in the euphotic zone (Arrigo et al., 2015).

Limitations exist in the models however, principally in the parameterisations that drive the thermodynamic exchange between seawater and ice. Thermodynamic interaction is typically parameterised with the 'three-equation parameterisation' (Hellmer and Olbers, 1989; Holland and Jenkins, 1999), which can be formulated as:

$$\rho_{fw} m_w L_i = \rho_i c_i \kappa_i \left.\frac{\partial T_i}{\partial z}\right|_b - \rho_{sw} c_{sw} u_* \Gamma_T (T_b - T_M) \quad (1)$$

$$\rho_{fw} m_w S_b = -\rho_{sw} u_* \Gamma_S (S_b - S_M) \quad (2)$$

$$T_b = a S_b + b + c p_b \quad (3)$$

$$u_*^2 = C_D {u'_M}^2 \quad (4)$$

Here, m_w is the melt rate (water equivalent), u_* is the friction velocity, T_b, S_b and p_b are the temperature, salinity and pressure at the ice base, T_M, S_M and u_M are the temperature, salinity and velocity at some specified distance from the ice base. In this ISOMIP+ application, the heat diffusivity into ice (κ_i) is set to zero (insulating ice), and the water speed explicitly includes a constant tidal offset, ${u'_M}^2 = u_M^2 + u_{tidal}^2$. The turbulent exchange coefficients for temperature, Γ_T, and salt, Γ_S, will be discussed throughout this paper. Other parameters are constants, as defined in Jenkins et al. (2010), with subscripts $_{fw}$ and $_{sw}$ referring to freshwater and seawater, respectively.

This approach sees widespread use and is the most commonly applied parameterisation (see for example Dinniman et al., 2015; Galton-Fenzi et al., 2012; Kusahara et al., 2017; Gwyther et al., 2014). The three-equation parameterisation divides the interface region into ice, ice–ocean interface and far-field ocean, and describes a conservation of heat equation (Eq. (1)) and salt equation (Eq. (2)) with fluxes across each boundary. The linearised freezing point temperature (Eq. (3)), a function of in situ salinity and pressure, closes the parameterisation and allows the equations to be solved for melt rate (as well as the temperature and salinity) at the ice–ocean interface. Turbulent processes that mix heat and salt from the ocean below to the ice interface are parameterised as turbulent exchange rates or velocities. The description of turbulent exchange is based on empirical evidence: sea ice observations (e.g. McPhee et al., 1987; McPhee, 1992) and laboratory experiments (Kader and Yaglom, 1972). Evidence from below the Ronne-Filchner Ice Shelf supports the three-equation parameterisation, but also suggests that a simplified parameterisation would fit the data equally well (Jenkins et al., 2010). Observations of double diffusive staircases beneath George VI Ice Shelf are an example where the three-equation parameterisation has been shown to not accurately solve for melt rate (Kimura et al., 2015). Davis and Nicholls (2019) showed that the law of the wall assumption, inherent in the three-equation parameterisation, does not hold at weak flow speeds.

This parameterisation has been applied to many ice–ocean models with different vertical configurations. Typically, the parameterisation is applied between the top model cell and the ice, and hence the location where the temperature to drive melting is sampled changes as a function of the vertical resolution. Likewise, the depth over which heat and freshwater fluxes from melt are released will change depending on vertical resolution. As a result, the simulated melt rate is often a direct function of vertical resolution. However, as will be discussed below, the temperature to drive melting can also be computed as an average over a model 'mixed layer' that may include more than one vertical grid cell, in which case the simulated melt may be a more complicated function of vertical resolution. Since the practical implementation of these parameterisations differs across model frameworks, the results of ice–ocean simulations with different models may respond differently to this vertical resolution dependency.

Turbulence generated by velocity shear in the momentum boundary layer is important for exchanging heat and salt to the base of the ice shelf. However, the shape that this momentum boundary layer takes is largely unconstrained except for a few sparse observations and recent high resolution modelling efforts (see Section 4.2). Almost all ice–ocean models adopt a simple parameterisation of the boundary layer, namely that the surface shear stress (τ_0) that drives turbulence is a quadratic function of a representative water velocity (U), $\tau_0 = \rho_{sw} C_D U^2$, where C_D is a dimensionless drag coefficient and ρ_{sw} is the ocean density. This 'quadratic drag parameterisation' can be written in terms of the friction velocity u_* as $u_*^2 = C_D U^2$. While the form of this parameterisation can be used for predicting stress using a variety of representative velocities (see Soulsby, 1983), the drag coefficient will be different for a different representative velocity (e.g. 'free stream velocity' at the edge of the boundary layer, depth averaged velocity, velocity at a specific depth). The location for the sampling of the representative velocity is unclear, and may also introduce a resolution dependency. For example, the 'free stream velocity' should be sampled at the edge of the boundary layer beyond the influence of interface friction, but this will change for different roughnesses and for different water velocities. In the presence of a strong upslope buoyant plume, which modifies the vertical velocity profile (e.g. Jenkins, 2016), the relevance of the free stream velocity to surface stress is also unclear. Likewise, while a 'depth-averaged velocity' (across the entire water column) may be feasible in shallow shelf seas, it is clearly not appropriate for overturning flow within an ice shelf cavity. Sampling the velocity at a chosen depth (which most models currently do) is susceptible to vertical resolution dependencies and should likely be acquired within the log-layer ($\mathcal{O}(1)$ m; Davis and Nicholls, 2019) requiring both a high vertical resolution at the ice–ocean interface and a C_D that is a function of distance from the interface.

Almost all ice–ocean models, including those used here, do not currently implement more complex controls on how momentum exchange is calculated (such as varying where the representative velocity is sampled due to surface roughness and ambient flows such as buoyant plumes) and so we note that this dependency exists but do not investigate it in more detail.

Results presented in this article were obtained using the experimental setup from the second Ice Shelf–Ocean Model Intercomparison Project, ISOMIP+ (Asay-Davis et al., 2016). However, this article is neither intended to be a detailed overview of ISOMIP+, nor a comprehensive overview of the main results from the ISOMIP+ experiment (see Asay-Davis et al., 2016). Instead, this article will explain key differences between a terrain-following vertical coordinate model (ROMS), a z-coordinate model (COCO) and an Arbitrary-Lagrangian–Eulerian vertical coordinate model (MPAS-O) within the ISOMIP+ framework. The effect of vertical resolution on melt rate, and the effect of implicitly and explicitly parameterised vertical mixing on ice–ocean models will also be investigated in the context of ISOMIP+ and ice–ocean modelling as a whole. This article will improve understanding of the differences in simulations that results from different model platforms. Recommendations will be made for future modelling and observational studies. However, this study, like ISOMIP+, is not designed to provide the correct answer for 'How ice–ocean interaction occurs and who is simulating this correctly'. Section 2 provides a brief overview of the ISOMIP+ common resolution and parameter (COM) experiments, and models participating in this study. Section 3 summarises selected ISOMIP+ results to illustrate the differences between different model configurations, while the impact of chosen vertical resolution is demonstrated across different model frameworks. In Section 4, the dependence on model vertical resolution is linked to vertical mixing processes and the implications for understanding modelling studies and designing future model simulations are discussed.

2. Experimental setup

The Marine Ice Sheet–Ocean Model Intercomparison Project (MISOMIP; A Climate and Cryosphere Project targeted activity[1]) describes a semi-idealised fjord-like bathymetry with a glacier and ice shelf. The intercomparison project will consist of an ice sheet component and an ice shelf–ocean component (ISOMIP+ Asay-Davis et al., 2016). The aim of MISOMIP is to aid in the validation and development of fully coupled ice sheet–ocean models, together with their constituent stand-alone components.

ISOMIP+ follows the precedent established by several previous idealised ice shelf–ocean modelling studies (Grosfeld et al., 1997; Holland et al., 2008; Losch, 2008; Little et al., 2008, 2009; Goldberg et al., 2012a,b; Kimura et al., 2013; Dansereau et al., 2014; Gwyther et al., 2015, 2016), and the original ISOMIP (Hunter, 2006). The aim of these experiments is to provide a test case for development of ice shelf–ocean model applications; explore and better understand ice–ocean interaction; and, compare different modelling frameworks and parameters. The specifications for ISOMIP+ outline five experiments with different initial and boundary forcing conditions, as well as (in two experiments) a time-varying ice geometry. ISOMIP+ is chosen as the experimental framework so as to facilitate easier comparison to results from other models in ISOMIP+, and those developed in the future.

The first three experiments in ISOMIP+, Ocean0, Ocean1 and Ocean2, use a steady-state ice geometry. They are designed to examine the response of basal melting and circulation within the ice shelf cavity to far-field ocean forcing. The first experiment, Ocean0, uses warm initial conditions throughout the cavity and continually restores at the northern boundary to the same initial conditions. Ocean1 is designed to examine the response to a warming ocean, and hence is initialised with cold oceanic conditions and has restoring at the northern boundary to warm conditions. Ocean2 is designed to examine the response to a cooling ocean, and hence is initialised with warm oceanic conditions and has restoring to cool conditions at the northern boundary. The details for these experiments are covered at length in Asay-Davis et al. (2016).

In this study, the experiment Ocean0 is chosen as the base of comparison for the different models. This is because the initial and restoring conditions allow for faster model spin-up than Ocean1 or Ocean2, with ocean conditions typically reaching a quasi-steady state in one to two years. However, in Section 3.4 we use the same geometry, but with cold initial condition and cold restoring conditions to simulate a cold cavity environment, with details given in Asay-Davis et al. (2016).

In ISOMIP+, interior vertical mixing is similar for each model with constant values of vertical diffusivity and viscosity. If the local stratification is unstable, vertical diffusivity and viscosity are increased to larger constant values. The experimental design excludes more complex parameterisations of vertical mixing, for example K-Profile Parameterisation (KPP Large et al., 1994) which includes a non-local surface boundary layer and instability from resolved vertical shear, unresolved double diffusivity and internal waves in the calculation of interior diffusivity and viscosity.

Vertical mixing at the ice shelf–ocean boundary region must be considered separately. For the z-coordinate models in ISOMIP+, the vertical resolution may not resolve the ice shelf–ocean boundary layer, particularly where melting produces a stably stratified and thin boundary layer (e.g. 12 m beneath melting sites on Pine Island Glacier; Stanton et al., 2013). This is also true for z-coordinate models in realistic applications, where computational efficiency does not allow for sufficient vertical resolution to resolve the ice–ocean boundary layer. As the boundary layer is not resolved, a separate parameterisation is generally employed. ISOMIP+ prescribes the boundary layer method similar to that described in Losch (2008). This is achieved by distributing meltwater released by basal melting down to a prescribed depth below the ice–ocean interface, which in Losch (2008) was equivalent to one full grid cell, but could be set to be several cells below, or indeed could be set to be independent of vertical resolution (e.g. MPAS-O). Likewise, the choice of where to sample the far-field temperature is generally at a certain depth below the ice shelf base (Kimura et al., 2013) or as the average down to the mixed layer depth. In this comparison, COCO and MPAS-O each employ unique boundary layer schemes, with MPAS-O using a modified Losch-style scheme. ROMS is configured to sample temperature and salinity at the top grid cell (generally ~1 m thick) and release meltwater into the top model cell, allowing the vertical mixing scheme to parameterise the transport of momentum and tracers downwards. More details of the boundary layer mixing schemes for each model are given in Table 1, Table A.1, and at relevant locations through the text.

Most modern models use transfer rates (turbulent exchange velocities for temperature γ_T and salinity γ_S) that vary as a complex function of velocity amongst other parameters, following McPhee et al. (1987). ISOMIP+ specifies a velocity-dependent formulation where the exchange velocities, γ_T and γ_S are linear functions of the friction velocity u_*, such that $\gamma_{T/S} = u_* \Gamma_{T/S}$, where the turbulent heat and salt transfer coefficients for temperature and salt, Γ_T and Γ_S, are assumed to be constant. Observations of turbulent exchange below sea ice offer support for this assumption (McPhee and Kottmeier, 1999). In the parameter studies that follow, we vary the transfer coefficient between experiments, to assess the impact of weaker to stronger turbulence.

2.1. Model descriptions

The Regional Ocean Modeling System (ROMS) is a 3D numerical ocean model developed for coastal ocean modelling studies (Shchepetkin and McWilliams, 2005). It uses a terrain-following vertical coordinate configured to provide higher resolution at the ocean surface and at the bathymetry ("s-coordinate"), to better resolve surface and bottom boundary layers, and lower resolution in the mid-depths. Modifications to ROMS allow for ice shelves (following Dinniman et al., 2007; Galton-Fenzi et al., 2012), with ice–ocean thermodynamic interaction from the three-equation melting/freezing parameterisation (Hellmer and Olbers, 1989; Holland and Jenkins, 1999). The geometry and chosen vertical scaling coordinate produced top-layer cells of thickness 0.5 m near the grounding line, 3 m at mid-ice shelf and 5 m near the ice front.

The Center for Climate System Research Ocean Component Model (COCO) is a z-coordinate, coupled ocean-sea ice model developed in partnership between the Japan Agency for Marine-Earth Science and Technology and the Atmosphere and Ocean Research Institute, the University of Tokyo. Like ROMS, COCO solves the primitive equation under the Boussinesq and hydrostatic approximations, and includes a steady-state ice shelf component (Kusahara and Hasumi, 2013). It has been used for modelling ocean-cryosphere interactions over the Southern Ocean (Kusahara and Hasumi, 2013, 2014; Kusahara et al., 2017). In the ISOMIP+ framework, COCO used a full-step representation for ice shelf draft, instead of a partial-step treatment (Adcroft et al., 1997). The full-step representation was used so that sampling of tracers and momentum is computed in the centre of each cell at a known, constant distance from the ice; with partial cells, this sampling would occur at arbitrary distances depending on the thickness of each partial cell. As configured for ISOMIP+ experiments, the vertical resolution was chosen as 20 m, and temperature and salinity in the uppermost grid cell were used to calculate basal melt rate. Meltwater fluxes were distributed by complete mixing with original tracer properties down to the prescribed depth; in the ISOMIP+ COM configuration, this is chosen as 20 m, equivalent to the vertical resolution. In this study, we also utilised COCO with higher vertical resolution of 2 m to examine the dependence of basal melt rate on vertical resolution and thickness of the prescribed mixed layer for fluxes. More details on the distribution of meltwater over the prescribed distance are given in the Appendix.

The Model for Prediction Across Scales: Ocean (MPAS-O; Ringler et al., 2013) is a Boussinesq, finite-volume primitive equation ocean

[1] http://www.climate-cryosphere.org/activities/targeted/misomip

Table 1
Model platforms compared in this study, and their respective vertical resolution dependencies.

Model	Flux mixing thickness	Tracer sampling distance	Resultant vertical resolution dependency
ROMS	Top layer	Top layer	Sampling and distributing fluxes both function of vertical resolution
COCO	Prescribed depth	Top layer	Sampling function of vertical resolution; flux over prescribed 'mixed layer' depth
MPAS-O	Prescribed depth	Prescribed depth	Averaging and distribution of fluxes over prescribed distance

model based on a horizontal mesh composed of Voronoi tesselation of near-regular hexagons, and an Arbitrary–Lagrangian–Eulerian (ALE) vertical coordinate (Petersen et al., 2014). In the ISOMIP+ experiments, the coordinate is z* (Adcroft and Campin, 2004) in the open ocean while beneath ice shelves it follows the ice draft (but not the seafloor, where layers are instead dropped as they intersect the bathymetry in a manner similar to z-level coordinates). Similar to Losch (2008), in most experiments, temperature and salinity for calculating thermal driving are found by averaging over cells within 10 m of the ice, and melt fluxes (heat and freshwater) are distributed based on an exponential profile, with a decay length scale of 10 m. Unless otherwise stated, the MPAS-O experiments presented in this paper are performed with 120 vertical levels (corresponding to 6-m resolution in the open ocean and 2–3 m below the ice shelf in the deeper parts of the cavity).

The ISOMIP+ specifications suggest tuning of the turbulent heat transfer coefficient Γ_T such that the spatial mean melt rates are $\sim 30\,\mathrm{m\,yr^{-1}}$. As a result, the Ocean0 results shown here are conducted with $\Gamma_{T,\mathrm{ROMS}} = 0.05$, $\Gamma_{T,\mathrm{COCO}} = 0.025$ and $\Gamma_{T,\mathrm{MPAS\text{-}O}} = 0.0194$. In the remainder of the text, values of Γ_T are assumed to be these values unless otherwise explicitly stated.

Note that in this study we will refer to ROMS configurations as having high vertical resolution within the ice shelf cavities and z-level models as having lower vertical resolution. We acknowledge that vertical resolution of either coordinate system can be refined to high or low resolution, but typically, resolutions are chosen in the aforementioned configuration. The benefit of terrain-following coordinate models for ice shelf–ocean modelling is that they can be easily configured to simulate thin cells near to the ice–ocean interface without losing computational efficiency. However, the remapping of the primitive equations to a sigma-coordinate system can produce errors in the horizontal pressure gradient (Shchepetkin and McWilliams, 2003), leading to spurious flows near steeper changes in water column thickness such as at the ice front (Galton-Fenzi, 2009). Generally, sigma-coordinate models employ smoothing to reduce this issue, which can remove finer details in bathymetry and ice draft. Z-level models do not suffer from this type of error. Lower vertical resolution in z-level models is chosen to maintain computational efficiency — to obtain high resolution at the ice shelf–ocean boundary layer, thin levels must be chosen from near the surface of the ocean down to at least 2500 m. However, an issue with z-level models is the misrepresentation of vertical mixing near step-like topography (as a result of a coarse z-coordinate), which is known to degrade bottom boundary layer plumes (Ezer and Mellor, 2004) but could also affect buoyant meltwater plumes. The impact of different representations of the meltwater plume (and how that affects horizontal properties of the plume) on the results presented here is unclear.

2.2. Resolution dependencies in the ice–ocean thermodynamic parameterisation

There are multiple vertical resolution dependencies in parameterisations of thermodynamic exchange in ice shelf–ocean models. All of these dependencies relate to how heat is moved between the ocean and ice, and the vertical distance over which this occurs. The Holland and Jenkins (1999) parameterisation assumes an ice–ocean boundary layer above an ocean mixed layer. The ocean mixed layer is assumed to be well mixed and to have well defined properties such as layer thickness and tracer quantities, as found in isopycnal models (e.g. Holland and Jenkins, 2001). Subsequent models have generally adapted this original parameterisation to calculate the amount of heat available for melting, the thermal driving. Here we refer to the thermal driving as the difference between the in situ freezing point at the ice–ocean interface and the temperature some depth below the ice–ocean interface which represents the 'ambient ocean'. This thermal driving will also be modified by fresh meltwater feeding back on the freezing point, and as such, is also implicitly a function of the ambient ocean salinity. This has led to problems such as where to sample the temperature and salinity that drive melting. In ROMS, these values are sampled in the top ocean cell, which may or may not match the original design of the three-equation parameterisation, depending on how thick the top ocean cell is compared to any ice–ocean boundary layer. In z-coordinate models that employ partial thickness cells, a simple boundary layer scheme calculates the thermal driving with the mean temperature over a prescribed distance from the ice (Losch, 2008). This prescribed distance likely does not match the ice–ocean boundary-layer thickness.

As a result, resolution dependency exists in the method for calculating the thermal driving and the method by which meltwater is released back into the model. The calculation of the thermal driving typically involves either sampling of temperature and salinity in the top model cell, or averaging across multiple cells. Meltwater fluxes can likewise be applied into the top model layer, or distributed (via mixing or fluxes) into a prescribed depth. We have chosen to refer to the depth over which tracers are sampled or averaged in the calculation of melt rate as the 'tracer sampling distance' (TSD), while the depth over which meltwater fluxes are mixed or distributed will be referred to as the 'flux mixing thickness' (FMT). The purpose of the rest of this paper is investigate how the parameterisation choices made for the tracer sampling distance and flux mixing thickness impact melt rate in different model frameworks.

In Table 1, the vertical-resolution dependencies for model platforms in this paper are shown, with more details given in Table A.1. In ROMS, thermal driving is sampled and meltwater fluxes are distributed into the top model layer. As a result, mixing immediately below the ice–ocean interface must be dealt with by the internal vertical mixing scheme. In COCO, meltwater fluxes are distributed over a prescribed depth, but thermal driving is sampled in the top layer. In MPAS-O, both the averaging of tracers for thermal driving and distribution of meltwater fluxes is over a chosen prescribed depth. In reality, tracer and momentum boundary layer thickness are a function of ocean and interface properties and thus will vary in space and time. It seems unlikely that they can be represented realistically by any fixed value.

3. Results

3.1. Differences in melting

The ISOMIP+ results of ROMS, COCO and MPAS-O are directly compared, to highlight similarities and differences. A metric for model comparison proposed for ISOMIP+ from Asay-Davis et al. (2016) was the area-averaged melt rate where the ice draft (the ice–ocean interface) is deeper than 300 m. We use this metric throughout the rest of the study focusing on the region below 300 m depth with areal extent shown by the black outlines in Fig. 1. In ISOMIP+, specifications called for the turbulent heat exchange coefficient Γ_T to be tuned such that the area-averaged melt rate was $\sim 30\,\mathrm{m\,yr^{-1}}$, however even for very high Γ_T, ROMS could not reach an area-averaged melt rate of $30\,\mathrm{m\,yr^{-1}}$. Melting is lower in ROMS by a factor of two compared to COCO and MPAS-O (Fig. 1) with approximate steady state melting of $13.5\,\mathrm{m\,yr^{-1}}$

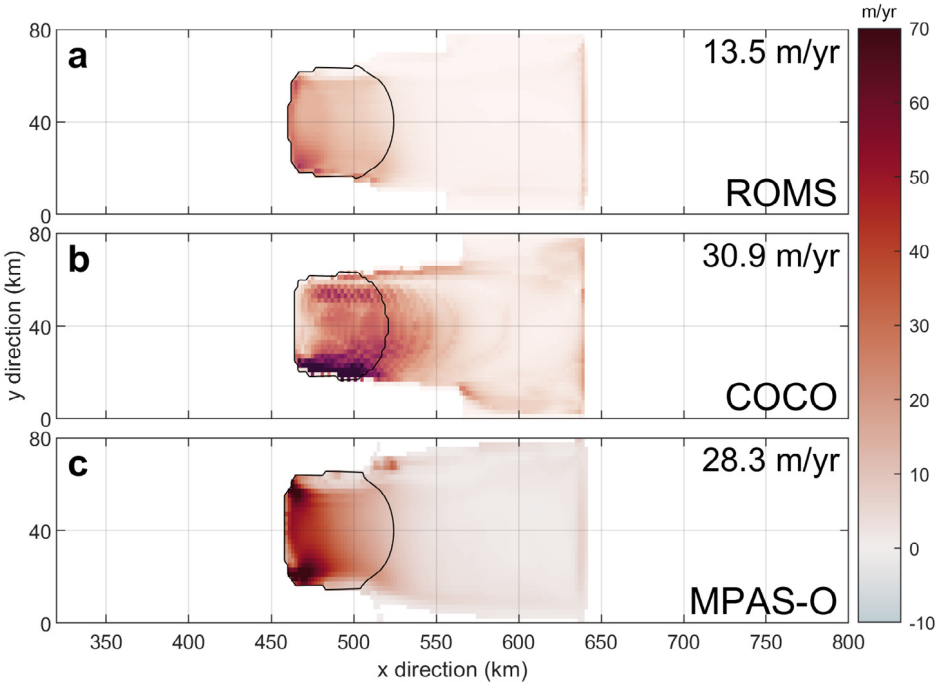

Fig. 1. Spatial pattern of time-averaged melt rate for (a) ROMS, (b) COCO and (c) MPAS-O. Ice deeper than 300 m below sea level is outlined with a black contour in each panel. Spatially averaged melt rates over this region are compared throughout the remainder of the paper. Melt rate is averaged over the last year of integration.

for ROMS, $30.9\,\mathrm{m\,yr^{-1}}$ for COCO, and $28.3\,\mathrm{m\,yr^{-1}}$ for MPAS-O. The similar spatial patterns and mean magnitude of melt rates between COCO and MPAS-O (compare Fig. 1b and c) is unsurprising given that ISOMIP+ models were purposefully tuned (by adjusting Γ_T) to reach a mean melt of $30\,\mathrm{m\,yr^{-1}}$. The fact that ROMS (Fig. 1a) displays less than half the mean melting of the other models will be shown to relate to its higher vertical resolution.

The spatial distribution of thermal driving ($T_* \equiv T_w - T_f$; difference between the ambient ocean water temperature (see definition for each model in Table 1), T_w and the in situ pressure freezing point T_f) at the end of the run shows similar differences (Fig. 2). ROMS again displays much weaker T_* across the ice shelf compared to both COCO and MPAS-O.

A vertical transect (at $y = 40$ km) through each model shows temperature conditions for the cavity and open ocean area (Fig. 3). The temperature distribution for each cavity is similar. The meltwater layer is easily observable in the COCO and MPAS-O results as it is relatively thick (see Fig. 3 insets). In ROMS, the meltwater layer adjacent to the ice shelf is thin and cold (for example at x = 500 km, −2 °C compared to −1.3 °C and −1.8 °C for COCO and MPAS-O, respectively). As we explore in the next section, the combination of the fact that ROMS computes melt based on ocean properties in the cells immediately below the ice and the low vertical mixing prescribed in ISOMIP+ for the ambient water column lead to lower thermal driving and reduced melting in ROMS compared to COCO or MPAS-O. Even after adding additional sources of mixing, including tides and a more complex vertical mixing scheme (KPP), vertical mixing near the ice–ocean interface was not strong enough to break down stratification and increase melt rates to match z-level models ('Typical configuration' experiments in ISOMIP+, which are not shown here).

3.2. ROMS melt rates as a function of vertical resolution

Here we show that weaker melting in ROMS is due to the thickness of the top layer over which thermal driving is calculated and meltwater is distributed by simulating melt rate at different vertical resolutions and across a range of heat transfer coefficients, Γ_T.

By decreasing the vertical resolution in ROMS, accomplished by reducing the number of vertical layers, melting increases. The ISOMIP+ experiments prescribe a low, constant rate of vertical mixing under stable stratification ($\kappa_{\mathrm{stab}} = 5{\times}10^{-5}\,\mathrm{m^2\,s^{-2}}$ for temperature and salinity). Because of this prescription, the mixed layer depth is effectively the thickness of the top model grid cell. As the average top cell thickness is increased, through $\Delta z_{\mathrm{TopAv}} = 1.1$ m (orange line; Fig. 4), 2.3 m (black line), and 4.8 m (yellow line), melting increases for any given Γ_T value. Above approximately $\Gamma_T = 0.01$, melting only weakly varies with increasing Γ_T, but across all Γ_T, melting increases with coarser vertical resolution.

In ROMS, any mixing from the top cell into the ocean below results from the internal mixing scheme. If there is limited mixing of heat from below and lateral advection of heat from upstream, the dependence of melt on resolution results from a lower total heat content being available to the base of the ice shelf with a thinner top layer.

To further explain why ROMS has lower melt rates, we present results where ROMS' vertical mixing parameterisation has been modified to mimic the lower resolution and the boundary layer scheme used in the ISOMIP+ z-level models. This modification adjusts vertical tracer diffusivity to a constant, high value (identical to the unstable convective adjustment diffusivity $\kappa_{\mathrm{unstab}} = 0.1\,\mathrm{m^2\,s^{-2}}$) from the ice surface down to a chosen prescribed distance (20 m in this case) below the ice surface (dashed curves in Fig. 4). Below this depth, diffusivity returns to the specified background rate κ_{stab}. As a result, tracer values sampled in the top cell will represent the mean value over the entire tracer sampling distance; in practice this is imposing prescribed tracer sampling distances *and* flux mixing thicknesses of 20 m, similar to the Losch-style scheme common in z-level models. Momentum diffusivity is left unmodified. While these results provide only qualitatively similar results to ISOMIP+ z-level models, they do show how ROMS simulates melting with lower vertical resolution near the boundary layer, while maintaining the same resolution through the rest of the model.

The modified vertical mixing configuration (dashed lines; Fig. 4) displays higher melting than the standard ISOMIP+ ROMS configuration (solid lines; Fig. 4). With the modified vertical mixing scheme, melt rates match the magnitude of melt rates of the predominately z-level

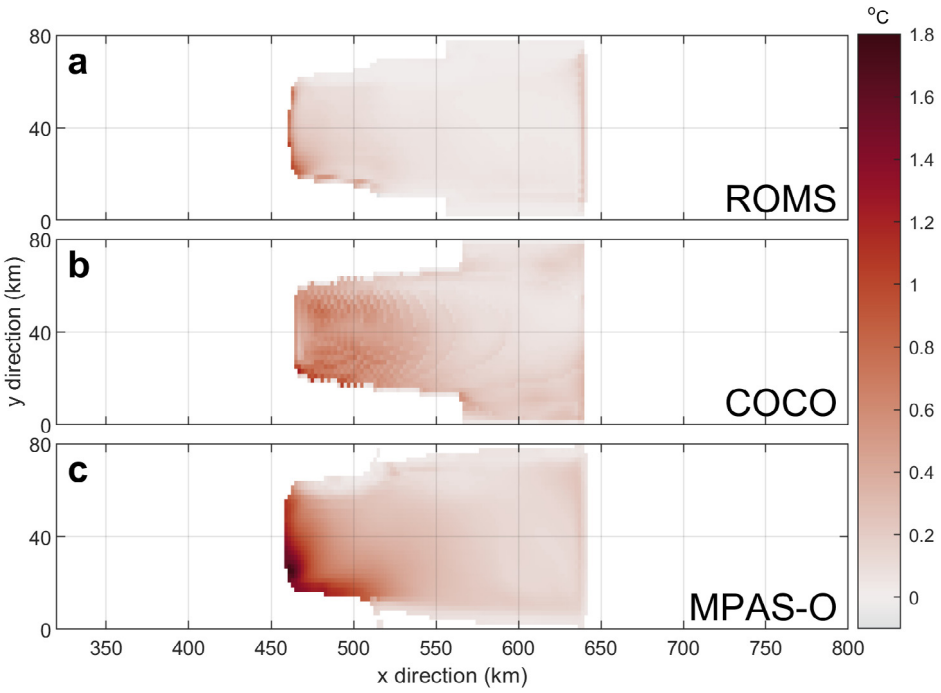

Fig. 2. Spatial distribution of mean thermal driving for (a) ROMS, (b) COCO and (c) MPAS-O.

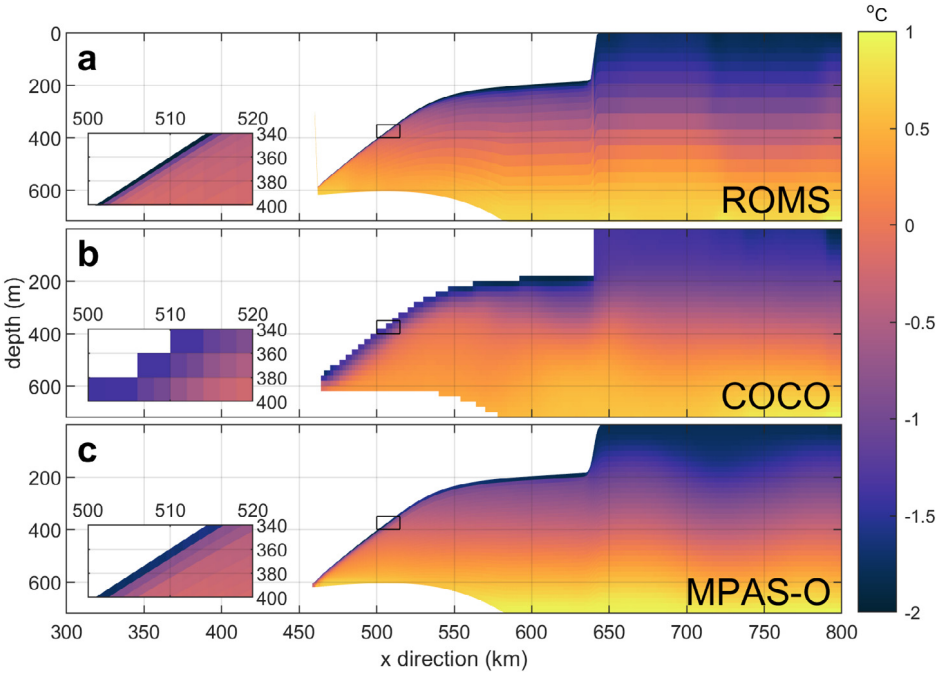

Fig. 3. Vertical transect through the centre of the cavity (y = 40 km) showing potential temperature for (a) ROMS, (b) COCO, and (c) MPAS-O. Inset in each panel shows the temperature distribution near to ice shelf–ocean interface, with location indicated with a black box.

models in ISOMIP+ (which are tuned to $30\,\mathrm{m\,yr^{-1}}$) for $\Gamma_T \sim 0.06$. Below melt rates of $8\,\mathrm{m\,yr^{-1}}$ (or $\Gamma_T = 2.5\times10^{-2}$), melt rates simulated with the default and modified mixing schemes follow the same dependency on Γ_T. This suggests that it is only at higher melt rates (above $8\,\mathrm{m\,yr^{-1}}$ in this case), that lower vertical resolution and the boundary layer scheme of Losch (2008) increase vertical heat transport from below into the top, relatively thin, ROMS model layer. At higher melt rates, the meltwater layer is spread out over the entire 20 m mixed layer by the modified mixing scheme, similar to the thicker prescribed depth in the Losch-style boundary layer scheme, but the higher turbulent transfer rate more effectively delivers this heat to the ice than in the case of low Γ_T and low melting. Note also that in the case of the modified mixing experiments, where both the flux mixing thickness and tracer sampling distance are set constant but Δz (vertical resolution) is changed, dependency of melting on vertical resolution is reduced (as we will also see in Section 3.5).

Lower melt rates in ISOMIP+ (e.g. as simulated by ROMS) are not as a result of a cooler cavity environment on the whole (see Section 3.1), rather, they result from the parameterisation of vertical mixing processes. For the same constant vertical diffusivity, deeper

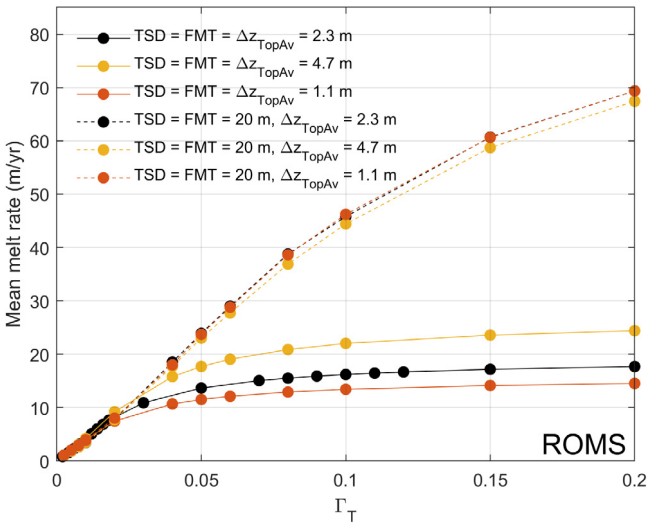

Fig. 4. Dependency of melt rate in ROMS on Γ_T, vertical resolution (spatially-averaged top layer thickness $\Delta z_{\mathrm{TopAv}}$) and the imposed depths for mixing fluxes (flux mixing thickness; FMT) and sampling tracers (tracer sampling distance; TSD). Orange, black and yellow markers and lines show mean simulation melt rates for a given vertical Γ_T and vertical resolution of 41, 21, and 11 layers, respectively. Solid curves are with the ISOMIP+ default vertical mixing, dashed curves are with enhanced vertical mixing in the top 20 m below the ice, mimicking lower vertical resolution at the ice–ocean interface.

mixing of fluxes and tracers will result in the ice–ocean interface being exposed to deeper and warmer waters, and thus higher melting. This is evidenced by the reduction of melt rates shown by COCO (a z-level model) if the z-levels and the pre-defined FMT are made nearly as thin as ROMS levels (see Section 3.3).

3.3. Impact of vertical resolution in other models

We utilised COCO with two vertical resolutions (a 2 m high resolution configuration, and the 20 m ISOMIP+ COM configuration) in order to examine the dependency of basal melt rate on the vertical resolution, thickness of the boundary layer, and the turbulent heat transfer rate, Γ_T. COCO employs a boundary layer scheme that is quite different from a Losch-style boundary layer scheme. In the case of COCO, tracers for melting are taken from the values in the top model cell. Meltwater flux is distributed uniformly over a Losch-style prescribed depth (though this depth is not necessarily identical to the vertical resolution), and the added meltwater is mixed completely with the original tracer properties.

The Ocean0 experiment with a one year integration is used to assess the dependency of basal melt on vertical resolution as simulated in COCO. We also performed a series of numerical experiments with the high vertical resolution configuration, changing Γ_T from 0.01 to 0.20, and the thickness of the simplified boundary layer over which meltwater is distributed (flux mixing thickness) from 2 to 40 m. The higher vertical resolution experiments were conducted to examine the dependency of basal melt on the FMT thickness, somewhat similar to that conducted with ROMS in Section 3.2.

The standard ISOMIP+ vertical resolution and mixed layer depth used by z-level models (black curves in Fig. 5) lead to strong melting that increases with Γ_T, as follows from the three-equation parameterisation where melt rate increases for increasing turbulent heat transfer. The relationship plateaus at high Γ_T, as increasing turbulence does not increase the maximum rate at which heat is delivered from the ocean interior (below the boundary layer). Comparing the standard ISOMIP+ configuration of COCO to a similar configuration but with tracers sampled at 2 m and fluxes distributed over a 20 m flux mixing thickness (yellow line) shows that sampling tracers closer to the ice shelf reduces melt rates (cf. black and yellow lines; Fig. 5a). Likewise, sampling thermal driving at 2 m and distributing fluxes within 2 m of the ice shelf (×10 the vertical resolution of the ISOMIP+ configuration) leads to much lower melt rates in COCO. In Fig. 5b, a similar experiment is performed in MPAS-O where tracer sampling distance and flux mixing thickness are explicitly varied with vertical resolution held fixed at 120 vertical layers (~2–3 m, see Section 2.1). The results are similar: decreasing the tracer sampling distance reduces melting (in fact, more so than in COCO) and additionally decreasing the flux-distribution depth further decreases melting. The blue line shows an additional experiment that was not possible in COCO. Tracers are sampled over the top 20 m but fluxes are distributed in the top 2 m, leading to an *increase* in melt rates. This increase likely results from a (partial) decoupling of melt fluxes and ambient tracers, where there is little feedback from melting at the ice–ocean interface on ambient properties far below, given the weak mixing. Furthermore, in the Ocean0 experiment, the deeper the ambient temperature is sampled for thermal driving, the warmer it will be because of the prescribed vertical profile of temperature (Fig. 3).

To further explore the dependency on flux mixing thickness, we ran a suite of experiments in COCO and MPAS-O with a constant tracer sampling distance (2 m) but with different imposed flux mixing thicknesses and Γ_T values, as shown in Fig. 6. In both models, a flux mixing thickness thinner than 10 m limits melting to a maximum of $\sim 30\,\mathrm{m\,yr^{-1}}$, even with high Γ_T values. The small Γ_T regime, where increasing the flux mixing thickness has negligible impact on melting, is larger for COCO ($\Gamma_T < 0.03$) compared to MPAS-O ($\Gamma_T < 0.01$), indicating the impact that different model frameworks have in the simulation of melting. However, for both models, choosing a thinner flux mixing thickness generally will reduce melt rates, and likewise for decreasing the turbulent heat transfer Γ_T. As in Fig. 5, there are qualitative similarities in the response of melting simulated by COCO and MPAS-O to changes in Γ_T and the FMT, but differences in the details are likely due to the different application of boundary layer schemes.

Through decreasing the flux mixing thickness, vertical fluxes in the z-level model COCO and the ALE model MPAS-O are made to resemble that of a terrain-following coordinate model. At high resolution with a thin mixed layer depth (2 m for both), increasing the turbulent heat flux Γ_T was insufficient to transport heat to the ice surface and reach the melt rates ($\sim 30\,\mathrm{m\,yr^{-1}}$) simulated by z-level models with coarse resolution for the same experiment. These results also show the complex and covariant impact that the flux mixing thickness and tracer sampling distance have in governing melt rates.

3.4. Resolution dependency in a cold cavity environment

The vertical resolution dependency existent in the melt parameterisation is not a function of the magnitude of thermal driving. However, given that many ice shelves interact with a colder ocean cavity, it is important to investigate how strongly the dependency manifests in a variety of different cavity environments.

Cold cavity simulations show that all three model platforms perform similarly in response to different vertical resolution settings (Fig. 7), with an increase in the flux mixing thickness and tracer sampling distance leading to increased melting in ROMS, COCO and MPAS-O. Again, a larger TSD than FMT (blue line; Fig. 7c) acts to partially decouple the calculation of melting from release of meltwater.

The main difference from a warm cavity environment is the lower magnitude of melting, which is to be expected for a reduced thermal driving. Also noticeable is a reduced spread in melt rates for different resolutions. This suggests that while the impact of vertical resolution dependency is in the same direction for a warm or cold cavity, the latter will exhibit a lower sensitivity to model choices. This could be expected from other modelling studies, where a warmed cavity exhibited disproportionately higher melting (e.g. Gwyther et al., 2016). In this study we focus on warm cavities, as the phenomenon we are studying is most impactful in this regime, but it is also important to quantify the effect for cold cavities.

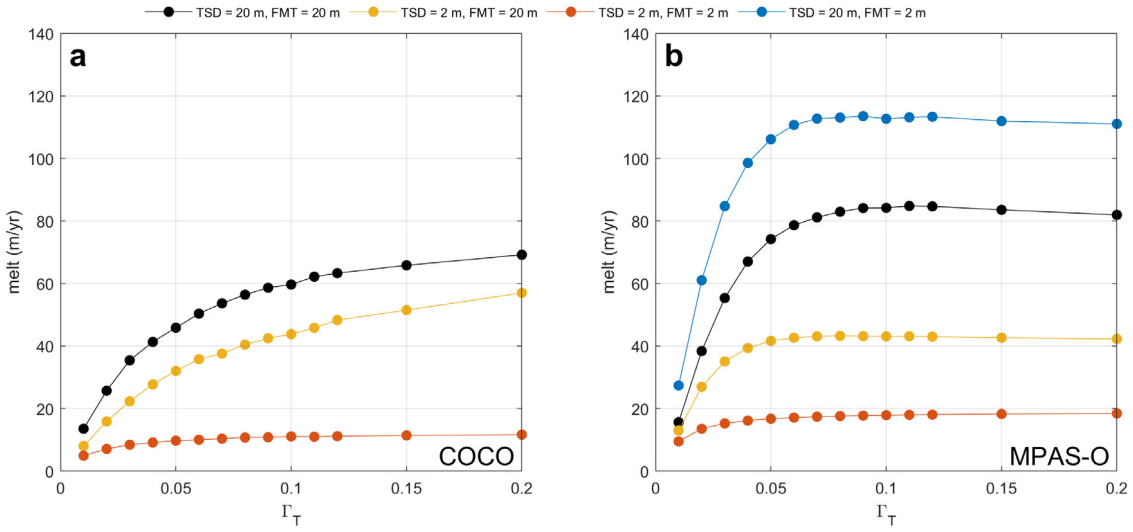

Fig. 5. Dependency of basal melt rate on Γ_T for different tracer sampling distance (TSD) and flux mixing thickness (FMT) parameters in (a) COCO and (b) MPAS-O. Taking the black curve as a reference point, the yellow curves show a reduction in melting from sampling tracers closer to the ice interface, and the orange curves show an additional reduction from distributing meltwater fluxes closer to the ice interface. In (b), the blue curve shows an *increase* in melting when fluxes are distributed close to the interface but tracers are sampled at greater depth in MPAS-O, likely resulting from a reduction in feedback between melting and ambient ocean temperature.

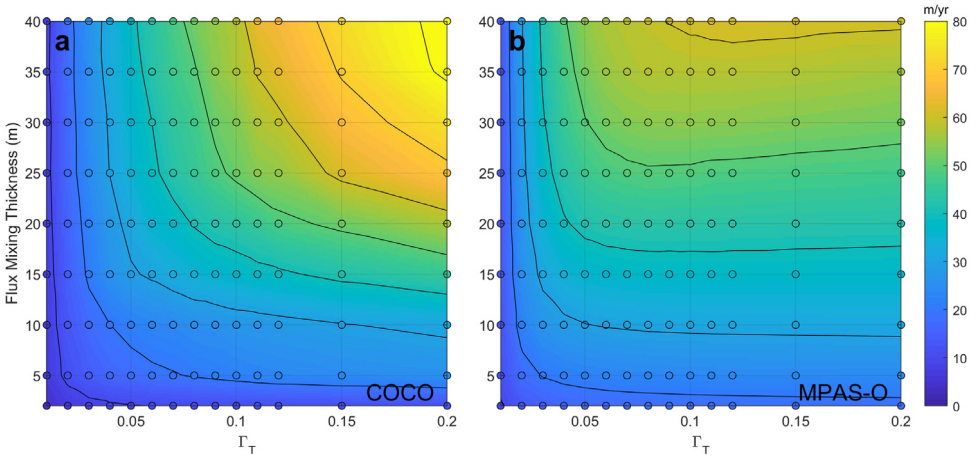

Fig. 6. Dependency of basal melt on Γ_T and flux mixing thickness in (a) COCO and (b) MPAS-O. Hollow circles indicate mean melt rate for a given Γ_T and flux mixing thickness, while colour map and contours show the interpolated relationship between flux mixing thickness, Γ_T and melt rate. The tracer sampling distance is held fixed at 2 m in COCO and at 20 m in MPAS-O.

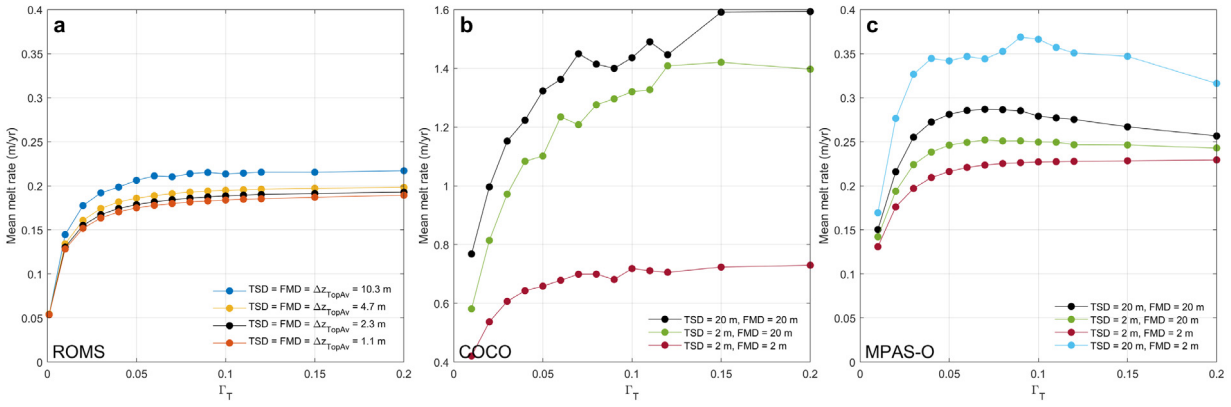

Fig. 7. Area averaged melting in a cold cavity environment for (a) ROMS, (b) COCO, (c) MPAS-O, under a range of turbulent transfer (Γ_T) values and choices of flux mixing thickness and tracer sampling distance. Note difference axis in panel b. In all panels, black lines are the ISOMIP+ default configuration.

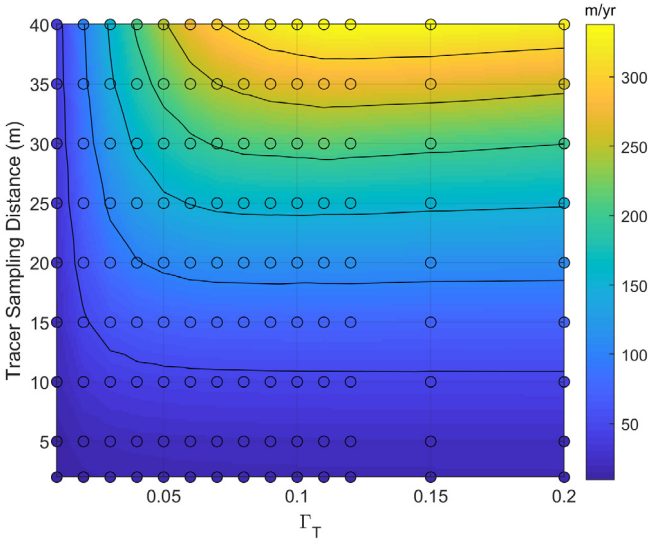

Fig. 8. Dependency of basal melt on Γ_T and the tracer sampling distance in MPAS-O. Hollow circles indicate mean melt rate for a given Γ_T and tracer sampling distance, while colour map and contours show the interpolated relationship between tracer sampling distance, Γ_T and melt rate. The flux mixing thickness is held fixed at 20 m.

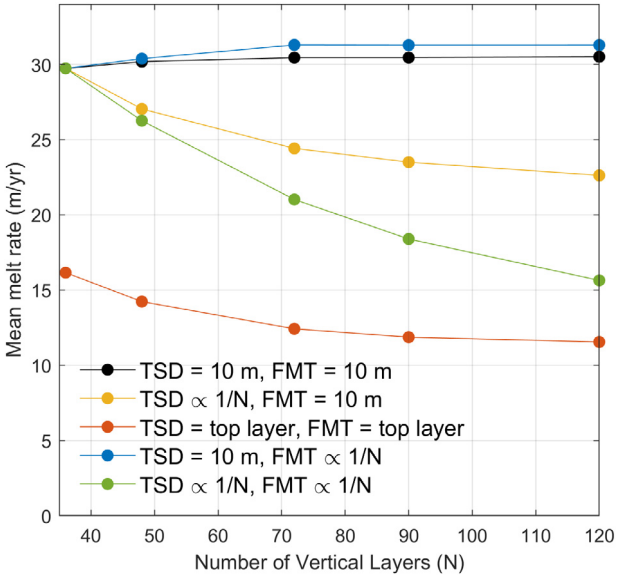

Fig. 9. Mean melt rate as a function of vertical resolution in MPAS-O for five experiments: tracer sampling distances and flux mixing thicknesses fixed at 10 m (black); TSD (yellow), FMT (blue) or both (green) varying in proportion to the mean vertical resolution (i.e. inversely to the number of layers (N) from 10 m at 36 layers to 3 m at 120 layers); and both TSD and FMT only covering the top layer (red). By default, COCO and most z-level models participating in ISOMIP+ behave like the green curve as vertical resolution varies, explaining why melt rates are a strong function of vertical resolution in these models. ROMS behaves more like the red curve (which asymptotes to the green curve at higher resolution), and MPAS-O also shows substantially lower melting in this configuration.

3.5. Separating the resolution-dependent response

MPAS-O employs a modified Losch-style boundary layer scheme, though it differs in details to Losch (2008). Similar to Losch (2008), MPAS-O samples tracers by averaging over a prescribed depth, but the distribution of meltwater fluxes into the prescribed depth is with an exponential profile (see details in Appendix), rather than uniformly as in Losch (2008). MPAS-O is uniquely able to separate out the impact of the flux mixing thickness and tracer sampling distance, as both parameters can be prescribed independently while holding the vertical resolution fixed (whereas the tracer sampling distance is implicitly linked to the vertical resolution in COCO).

Fig. 8 shows that, in MPAS-O, the dependence of melting on the tracer sampling distance is much stronger than it is on flux mixing thickness (Fig. 6b). Assuming this strong dependence also holds for z-level models like COCO, this makes it difficult to compute melt fluxes that are independent of vertical resolution, given that the tracer sampling distance is constrained by the (typically coarse) vertical resolution, as we discuss in Section 4.1. When tracer sampling distances are comparable to (or less than) flux mixing thicknesses (20 m in Fig. 8), meltwater mixes deep enough to feed back on the thermal driving, thereby throttling melting. At large tracer sampling distances compared to the flux mixing thickness, parameterised melt processes do not mix deep enough to feed back on the thermal driving, leading to melt rates that are likely unrealistically large.

To get a better handle on how melt rates vary with vertical resolution, we also performed a series of experiments where we varied the number of vertical layers in MPAS-O between 36 and 120 with various choices of how the tracer sampling distances and flux mixing thicknesses varied with resolution (Fig. 9). In one experiment (the black curve), both TSD and FMT were held fixed at 10 m. In three of the remaining experiments, the tracer sampling distance (yellow), flux mixing thickness (blue) or both (green) vary in proportion to the resolution (from 10 m at 36 layers to 3 m at 120 layers). In the final experiment, both depths cover only the top layer (similar to the typical approach in ROMS). The first interesting conclusion from these experiments is that a melt rate with little sensitivity to resolution can be achieved in MPAS-O with the tracer sampling distance held fixed and the flux mixing thickness either held fixed or varied in proportion to resolution. As we will discuss in Section 4.1, this solution on its own is not very satisfactory because there are not clear, physical grounds for choosing a single, spatially constant value for these depths.

These results are consistent with those from ROMS shown in Fig. 4. By default in the Ocean0 experiment, ROMS' behaviour is similar to the red curve: melt rates are small and are further reduced with increasing resolution because both tracer sampling distance and flux mixing thickness cover only the top cell. With mixing modified to mimic lower vertical resolution and the Losch-style boundary layer scheme, ROMS behaves more like the black curve, showing melt rates that are nearly independent of resolution. Z-level models like COCO tend to follow the green curve as resolution varies (the coarse-resolution limit for the COCO experiments is shown by the black curve in Fig. 5a, while the high-resolution limit is shown in orange). A major difference is that ROMS is typically used at resolutions comparable to the right-hand side of Fig. 9 while COCO and other z-level models typically operate at resolutions even coarser than MPAS-O on the left-hand side.

4. Discussion

4.1. Relationship between dz and melt

In Section 3.1, we have shown large differences in basal melt rate among the models, particularly with COCO (a z-coordinate model) and MPAS-O (with its terrain-following top coordinate) compared to ROMS (with its terrain-following coordinate). However, in Fig. 3 the broad-scale distribution of heat within the cavity is approximately similar. The markedly different melt rates displayed by ROMS compared to COCO and MPAS-O are as a result of cooler conditions confined to the boundary layer region (see insets in Fig. 3).

In realistic simulations, melt rates can be tuned to match observations, meaning that fundamentally different models could simulate the same mean melt rate with different tuning and model set up. Even in such cases, melt rates could evolve quite differently between models in response to changes in ocean forcing or ice-shelf geometry, as will

be explored in analysis of the full set of ISOMIP+ results. This study explored changes in ocean forcing only in a limited way and used only three models, so we are not able to make broad claims about how model resolution and other modelling choices might affect sensitivity to ocean forcing. Nevertheless, our results suggest a strong sensitivity of melt rates to the choice of vertical resolution, discretisation and boundary-layer parameterisation that could reasonably be expected to affect the sensitivity of melt rate to changes in ocean forcing. As shown in Fig. 2, these choices likely also affect the pattern of melting, with implications for coupled ice sheet–ocean dynamics, processes that will be explored in analysis of the MISOMIP1 experiments (Asay-Davis et al., 2016). One option for tuning models to the same mean melt rate is by varying the turbulent exchange coefficients. It seems plausible that models tuned with very different turbulent exchange coefficients to arrive at the same mean melt rate would have significantly different sensitivity to changes in thermal driving and/or ocean velocity.

The basal melt dependence on vertical discretisation results from the treatment of the distribution of meltwater and the calculation of the thermal driving. Given that these choices are often fixed in the model code, it follows that the choice of model framework will have a large impact on simulated melting. In the z-level models following the ISOMIP+ COM configuration, melt fluxes are distributed over a specified and fixed 'mixed layer depth' following Losch (2008), equivalent to at least one full vertical grid cell thickness (~10–20 m). Likewise, the temperature and salinity used to calculate the basal melting are also averaged over this prescribed depth. In a terrain-following model, the thickness of the layer along the ice shelf base depends on the water column thickness, and so the typical thickness for the uppermost cell in the grounding line region is less than a few meters. In ROMS, the meltwater is distributed into the thin, top layer of the model. Since basal meltwater is fresh and less dense, it stabilises the water column under the ice shelf. Stable vertical profiles of temperature and salinity reduce the magnitude of basal melting through regulating turbulent upward heat flux to the uppermost grid cell where thermal driving is calculated.

The distribution of meltwater into the upper water column is the first vertical-resolution dependency in both ROMS and COCO. In ISOMIP+, mixing from the ice–ocean boundary layer into the ocean below is described by distributing tracer fluxes either into the top layer or over a predefined mixed layer depth. Heat and freshwater are distributed into the top layer (as in ROMS) or are fluxed into the flux mixing thickness (20 m for models with a Losch-style scheme in ISOMIP+), with a chosen profile (e.g. exponentially decaying as in MPAS-O or evenly mixed over the flux mixing thickness as in COCO). ROMS experiments simulating a lower vertical resolution boundary layer selectively increased mixing rates for heat and meltwater across the top 20 m of ocean, effectively producing the uniform properties of the top cell in a coarse resolution model. The increased vertical diffusivity mixes more heat into the cell closest to the ice shelf, reduces stratification from a meltwater layer and drives stronger melting. In idealised (e.g. ISOMIP experiments with MITGCM; Losch, 2008) and realistic (e.g. circum-Antarctic experiments in MITGCM; Schodlok et al., 2016) z-level models, maximum melt rates have been shown to increase with coarser vertical resolution, which is attributed to increased vertical mixing, decreased representation of the meltwater layer, and more heat closer to the ice shelf (Losch, 2008; Schodlok et al., 2016). In contrast, a terrain-following coordinate model that distributes meltwater fluxes into the thin, top model layer relies on the ocean vertical mixing parameterisation to mix meltwater downwards from the interface. Any well mixed layer will be calculated internally by a choice of vertical mixing scheme such as KPP. In the ISOMIP+ ROMS experiments, with constant interior vertical mixing and the absence of other sources of mixing (e.g. tides or increased surface energy input due to stress between the ice shelf base and a rapidly moving buoyant plume), meltwater released into the top model layer forms a buoyant insulating layer, leading to lower melt rates than in the case of other ISOMIP+ models despite broadly similar cavity environments.

The sampling depth of tracers for the calculation of melting is the second vertical-resolution dependency. The calculation of the thermal driving requires the sampling or averaging of temperature and salinity tracers. The location at which these tracers are sampled will impact the thermal driving. In a model with a Losch-style scheme (e.g. most z-coordinate models), thermal driving is usually calculated based on the average temperature and salinity values down to a prescribed mixed layer depth, typically equal to the vertical cell thickness (chosen as 20 m in ISOMIP+). In contrast, ROMS calculates thermal driving with the temperature and salinity in the top model layer. This produces a dampening of thermal driving due to sampling these tracers in the region where meltwater is also released. Conversely, when fluxes are distributed close to the ice but thermal driving is sampled over a larger depth, the feedback between meltwater release and thermal driving becomes partially decoupled. In this scenario and with low vertical mixing (such as these ISOMIP+ experiments), thermal driving will be increased and melt rates will be higher (e.g. blue curve in Fig. 5b).

In a warm cavity, the nonlinear relationship between thermal driving and melting (as a result of feedback processes like increasing buoyant overturning) leads to an exaggerated response to changes in resolution. The cold cavity regime is more linear, and the melting responds as a weaker function of the length scales introduced into the parameterisation. Modellers studying warm cavity ice shelves should therefore be particularly aware of the vertical resolution dependency, and how it might manifest with each vertical coordinate system.

In order to represent physical processes on a discrete grid, choices must be made about vertical resolution. A coarser grid will result in a greater depth being represented by a single tracer value, meaning that a coarser resolution is roughly equivalent to a strong vertical mixing over the thickness of the cell if that same thickness was represented by multiple layers. In other words, implicit mixing or homogenisation of fine-scale features within the cell thickness results from the vertical discretisation process. A higher vertical resolution and thinner layers will result in less implicit mixing. In the context of ISOMIP+, a high resolution ROMS simulation with thin vertical layers will represent a thin meltwater layer, and warmer water below. Given the choices of FMT and TSD in ROMS, this will lead to a lower melt rate than if a coarser resolution were used that homogenised the meltwater layers with warmer water below. In contrast, a z-coordinate model with coarser resolution (e.g. 20 m vertical cells) will homogenise meltwater with water below, leading to a higher melt rate. Models like MPAS-O that average "far-field" tracers for the ice–ocean boundary conditions and distribute fluxes over several vertical layers essentially treat the ice–ocean boundary layer as if the model had a coarser resolution, leading to melt rates comparable to z-level models. It does not seem possible to tune ROMS to reach the specified 30 $\mathrm{m\,yr^{-1}}$ mean melt rate, with the forcing conditions and tuning parameters prescribed in ISOMIP+, without a coarser vertical resolution or implementation of a new boundary layer scheme. It is in this sense that the melt rate in ROMS is lower than in other models, however, this comparison is given with caution, as the correct value for melting is unknown. Further observations are required to improve understanding of the boundary layer beneath ice shelves under different topographic, oceanographic and buoyancy conditions.

4.2. Towards vertical resolution independent parameterisations

Limitations in the current treatment of the ice shelf–ocean boundary layer that lead to resolution dependency in melt rates are well known (Dinniman et al., 2016; Schodlok et al., 2016; Asay-Davis et al., 2016). While we have demonstrated more thoroughly the reasons and limits of this dependency, there remains much uncertainty in how the impact of vertical-resolution dependency will manifest in more realistic models of ice shelf–ocean interaction. Given the important role of ice shelf–ocean models in forming accurate projections for future sea level rise, this major uncertainty must be addressed. Furthermore, as

computational power increases, there will likely be a move to higher vertical resolution. However, until the full spectrum of turbulent processes can be explicitly resolved, parameterisations of processes in the surface boundary layer will need to evolve with the increasing vertical resolution. While this article is not the appropriate forum to introduce a new parameterisation, we can indicate future research directions that may lead to improved simulation of the ice shelf–ocean boundary layer.

Understanding the structure and mechanisms that govern thermodynamic and momentum exchange at the ice shelf–ocean boundary layer are limited by the paucity of observations and the spatial heterogeneity of ice shelf–ocean interactions. Using turbulence, velocity and temperature observations beneath Larsen C Ice Shelf, Davis and Nicholls (2019) showed that in weak flow conditions the log-layer (the inner region where the 'law of the wall' applies) is relatively thin (<2.5 m thick). As a result, sampling velocity outside of the log-layer, such as in models with thick vertical layers ($\mathcal{O}(10)$ m), while still using a quadratic drag parameterisation (that employs a C_D tuned for sampling within the log-layer), will lead to a significant difference in the magnitude of the friction velocity and melt rates (Davis and Nicholls, 2019). Even in models with high vertical resolution, the use of constant values of C_D (e.g. Jenkins et al., 2010) is not appropriate when velocities are sampled within the log-layer, in which C_D should depend on the distance from the ice–ocean boundary. Beneath Pine Island Glacier, within a channelised region of high basal melting, there was an observed mismatch between the altimeter measure of ice retreat and that inferred from salt fluxes (Stanton et al., 2013). This possibly indicates the presence of strong lateral advection moving salt fluxes from upstream, but it should also be noted that the nature of turbulent mixing at the ice shelf–ocean interface remain unknown and unquantified. Beneath McMurdo Ice Shelf, temperature and salinity measurements indicate a complex and varying vertical tracer profile (Robinson et al., 2010), contrary to a 'mixed layer' which provides the ambient properties for calculating thermal driving in the three-equation parameterisation. Beneath Ross Ice Shelf, a co-located ice penetrating radar site and a mooring allowed a robust assessment of the parameterisation, showing that in the situation with a tracer boundary layer which displays a thermal gradient ('less well mixed'), the melt rate dependency on temperature, as expected from Holland and Jenkins (1999), degrades (Stewart, 2017). Beneath George VI Ice Shelf, observations of diffusive–convective thermohaline staircases directly contradict assumptions of a turbulent boundary layer (Kimura et al., 2015). Furthermore, in complex conditions of supercooling, basal freezing, and a destabilising buoyancy flux, the robustness of current parameterisations is even less well known as suggested in observations (e.g. Robinson et al., 2014) and modelling studies (e.g. Rees Jones and Wells, 2018). Likewise, basal roughness (from microscale scallops (e.g. Bushuk et al., 2019) to sub-grid scale channels) affects a stress though the upper ocean to form a momentum boundary layer and impact melting. Observations of the sub-ice shelf surface are limited (e.g. Robinson et al., 2017) and the impact on melting has not been explored extensively (e.g. Gwyther et al., 2015).

The three-equation formulation assumes only vertical fluxes (across the boundary layer and into the ice shelf) without any net horizontal fluxes. However, simplified theoretical models by Jenkins (2016) show that, with a sloping interface and a buoyant plume, a steady state in the boundary layer could only be reached if spatial gradients were present in properties such as temperature or horizontal velocity. This, in turn, impacts assumptions of zero net horizontal heat and salt fluxes with further implications for how vertical transport through the boundary layer is parameterised. The three-equation parameterisation also assumes low stratification and a simple relationship between flow in the boundary layer and stress at the surface (quadratic drag law). However, in reality, observations suggest that complex stratification can exist below ice shelves (Kimura et al., 2015). Also, the optimum choices of U and C_D in the quadratic drag parameterisation are unclear. In a weak flow regime beneath Larsen C Ice Shelf, the friction velocity has been shown not to be related to the flow speed by a constant coefficient (Davis and Nicholls, 2019), as the quadratic drag law would predict. Further, it is likely that the constant value for C_D used in the MISOMIP experiments and many other ice–ocean models, is not consistent with the sampling location for velocity at either low or high vertical resolution.

Laboratory experiments show that features present at sub-grid scales such as variability in ice slope will impact melting (McConnochie and Kerr, 2018), but melt rates will depend on whether the ice–ocean boundary layer is turbulent or still largely laminar in nature (Magorrian and Wells, 2016; Gayen et al., 2016). One key feature that has been diagnosed in both laboratory experiments and high resolution modelling, is that assumptions made about the viscous sublayer (present within $\mathcal{O}(1\,\text{mm})$ from the ice) in Holland and Jenkins (1999) may not hold in all cases. Experimental testing has shown that there is a transition from a convectively controlled sublayer at lower water speeds to a shear-controlled sublayer. In the case of the former, melting is independent of fluid velocity, and an empirical relationship is proposed to describe this regime (McConnochie and Kerr, 2017). High resolution modelling and laboratory studies can help to improve ice shelf–ocean models through providing more appropriate parameterisations for the different turbulence regimes.

The importance of the transition from laminar to a turbulent boundary layer regime has also been shown in high resolution modelling. The nearly laminar regime is characterised by lower fluid velocity, higher stratification and hence lower melt rates as compared to the turbulent regime where higher turbulence (formed through strong velocity shear or buoyant flow along a steeply sloping ice shelf base) drives a well mixed boundary layer and higher melting. The degree of ice shelf slope, basal roughness, stratification and velocity shear will control the formation of a turbulently mixed boundary layer and hence whether the three-equation parameterisation produces representative results (Mondal et al., 2019; Vreugdenhil and Taylor, 2019). While modified melt rate parameterisations have been suggested for the regime transition from laminar and intermediately turbulent to fully turbulent, the application into regional ocean models needs to be more carefully considered. This is primarily due to the coupled nature of the problem, where ocean conditions drive melting which in turn influences the ocean conditions, and the demonstrated sensitivity to model choices such as where to sample tracers for thermal driving and where to release meltwater. Again, high resolution modelling is critical for providing parameterisations, independent of vertical resolution, that describe heat and salt transfer to the ice interface. These parameterisations must include the viscous sublayer and transport across the remainder of the boundary layer under a range of buoyancy conditions (stably stratified from melting or unstable convection from refreezing) and turbulence conditions (including diffusive–convective layers, laminar flow or fully developed turbulence).

However it is not enough to just provide new values (or even functional forms) of vertical heat and salt fluxes, Γ_T and Γ_S. Rather, a new parameterisation needs to feed into the vertical mixing scheme used in the ocean interior (e.g. KPP) by modifying the vertical diffusivities and viscosities in the sub-ice shelf boundary layer. Critically, for there to be no vertical resolution dependency, there must be a smooth transition between the parameterised unresolved boundary layer diffusivities and those used in the vertical mixing scheme for the resolved portion of the boundary layer.

5. Conclusions

We have demonstrated how the commonly used parameterisation for ice shelf–ocean thermodynamic interaction performs under different model frameworks. The methods for implementing this parameterisation, in particular how the tracers that drive melting are sampled and how meltwater fluxes are distributed, vary between different frameworks. Some models assume a relatively thick (e.g. ~20 m) 'mixed

layer' with a prescribed, non-varying thickness, while others using finer vertical resolution rely on explicit mixing from vertical mixing schemes such as KPP. However, though the methods for implementing this parameterisation vary between models, all either suffer from one of two problems; either an implicit dependency between melting and the vertical resolution of the model, or an arbitrary, constant choice of the flux mixing and tracer sampling distances with no physical basis.

These results also illustrate that previous modelling studies must be understood in the context of the chosen modelling framework and choices for how the melting parameterisation is implemented (i.e. flux mixing thickness and tracer sampling distance). The results above suggest that for a similar ocean environment and vertical turbulence parameterisation, ROMS may produce lower melt rates than a coarser resolution, z-level or ALE model. The most 'realistic' result is still unknown, as we have such limited observations of the sub-ice shelf environment.

Further investigation is required to understand the physics and processes that govern this transfer of heat and salt from the ocean outside the boundary layer into the ice. The parameterisations that develop from the improved understanding of this region must better capture the transfer of heat and salt across the unresolved portion of the ice–ocean boundary region, without a resolution dependency. Furthermore, it must achieve a physically based representation of the vertical heat and salt fluxes in the boundary layer that smoothly match with the fluxes imposed by the sub-grid-scale vertical mixing scheme in the resolved portion of the upper water column. This will be achieved through laboratory experiments and high-resolution modelling studies (e.g. Large Eddy Simulations or Direct Numerical Simulations) in combination with observations under a variety of basal conditions of the nature of turbulence and the rates of heat and salt transfer in the boundary layer.

Declaration of competing interest

The authors declare that they have no known competing financial interests or personal relationships that could have appeared to influence the work reported in this paper.

CRediT authorship contribution statement

David E. Gwyther: Conceptualization, Methodology, Software, Writing - original draft. **Kazuya Kusahara:** Conceptualization, Methodology, Software, Writing - original draft. **Xylar S. Asay-Davis:** Conceptualization, Methodology, Software, Writing - original draft. **Michael S. Dinniman:** Software, Supervision, Writing - original draft. **Benjamin K. Galton-Fenzi:** Supervision.

Acknowledgements

The authors thank 3 anonymous reviewers and Stefanie Mack for insightful critique that improved this manuscript. Research was supported by the Australian Research Council's Special Research Initiative for Antarctic Gateway Partnership (Project ID SR140300001). This research was undertaken with the assistance of computing resource grants *gh9* and *nk1* from the National Computational Infrastructure (NCI), which is supported by the Australian Government. Support for Xylar Asay-Davis was provided through the Scientific Discovery through Advanced Computing (SciDAC) program funded by the US Department of Energy (DOE), Office of Science, Advanced Scientific Computing Research (ASCR) and Biological and Environmental Research (BER) Programs as well as BER award No. DE-SC0013038. MPAS-O simulations were conducted at the National Energy Research Scientific Computing Center (DE-AC05-00OR22725).

Appendix. Details of model configuration

ROMS

ROMS uses an Arakawa C-Grid, with u- and v-velocities located on the cell east/west and north/south faces, respectively, and tracers located in the center of each grid cell (rho-point). Velocities at rho-points are calculated as the average of the velocities at adjacent u-/v-points. The momentum boundary condition is a quadratic drag law, which computes a friction velocity from the velocity magnitude in the top model layer.

Thermal driving is calculated (following Eqs. (1)–(4)) using temperature and salinity in the top model layer. Likewise, melt water release is captured through a 'virtual' salt flux into the top model layer. ROMS uses a terrain-following vertical coordinate where the distribution of layers here has been selected to provide a sigmoidal distribution. As a result there is an increased layer density at the top and bottom of each water column. Beneath the ice shelf, typical top layer thickness values are shown in Supplementary Table A.1.

COCO

COCO uses an Arakawa B-Grid and the u- and v-velocities are defined at the four corners. The tracer point is located in the centre of each grid cell. Velocities at rho-points are calculated as the average of the velocities at the adjacent velocity points.

COCO uses the temperature and salinity in the uppermost grid cell to estimate basal melt rate, and thus TSD is linked to the vertical resolution. After diagnosing the basal melt rate, COCO distributes the basal meltwater (in the form of a tracer tendency e.g. $\frac{dT}{dt}$) to the prescribed layers (FMT) to conserve heat, salinity, and freshwater, following Eq. (A.1) with parameter values from Table 4 in Asay-Davis et al. (2016). The re-estimated tracer values, ϕ', are calculated as

$$\phi' = \frac{(\eta + \Delta z_{ktop})\phi_{ktop} + \sum_{k=ktop+1}^{k'} \Delta_k \phi_k + \alpha}{\eta + \Delta\eta + \sum_{k=ktop}^{k'} \Delta z_k}, \tag{A.1}$$

where

$$\alpha = \begin{cases} \Delta\eta(T_f - \frac{L}{c_w}) & (\phi : \text{temperature}) \\ 0 & (\phi : \text{salinity}) \end{cases}$$

Here, ϕ is the original tracer (temperature and salinity), Δz is the vertical grid thickness, k is the grid index of the uppermost cell under the ice shelf, k' is the grid index of the bottom cell in the FMT, η is sea level height, and $\Delta\eta$ is sea level change caused by basal melting/freezing.

In the lower resolution COM simulations, the FMT is the same as the cell size of the uppermost grid cell (20 m). In the series of higher vertical resolution experiments, we change the prescribed distance over which fluxes distributed from 2 m to 40 m to see the dependency on the basal melting, while TSD is kept to the uppermost grid size of 2 m.

Other parameters used are listed in Supplementary Table A.1.

MPAS-O

MPAS-O uses an Arakawa C-Grid, with normal velocities located on the edges of polygonal cells (typically hexagons). Velocity magnitudes at cell centres are computed based on an area-weighted average of the square of the normal velocities on edges in the top model layer. The momentum boundary condition at the ice-shelf base is a quadratic drag law, which uses a friction velocity computed from the velocity magnitude in the top model layer.

Layer thicknesses in MPAS-O are initialised to maintain a Haney Number (Haney, 1991) below 5. This is accomplished by thickening layers in regions of steep ice slope, notably the calving front, but otherwise allowing them to thin as the water column thins. Unlike ROMS, the bottom coordinate in MPAS-O does not follow the terrain. Instead, layers are 'dropped' where they fall below the bathymetry in a similar fashion to z-level models. Layer thicknesses are a minimum 1 m, and the water column is not allowed to become thinner than three layers (therefore 3 m) thick. Layer thicknesses vary with the

Table A.1
Further details of model setups are given. Δz is the range of thicknesses of the top layer (for the under-ice region) for different model configurations. ν_C is the vertical tracer viscosity for both stable ($_{\text{stab}}$) and unstable ($_{\text{unstab}}$) stratification. Likewise, κ_C is the vertical tracer diffusivity for both stable ($_{\text{stab}}$) and unstable ($_{\text{unstab}}$) stratification. Details of the FMT and TSD schemes are given, as well as the manner in which u_* (friction velocity) is calculated. The momentum boundary condition parameterisation for each model is given, along with the corresponding drag coefficient, C_D.

	ROMS	COCO	MPAS-O
Grid type	C-grid	B-grid	C-grid
Δz range (COM experiments)	mean: 4 m, min: 0.3 m, max: 9 m (21 layers)	20 m (36 levels)	mean: 10.8 m, min: 1.2 m, max: 19 m (36 layers)
Δz range (other config)	mean: 19 m, min: 1 m, max: 43 m (6 layers);	2 m (360 levels)	mean: 8.2 m, min: 1.1 m, max: 15 m (48 layers);
	mean: 9 m, min: 0.6 m, max: 19 m (11 layers);		mean: 5.8 m, min: 1.1 m, max: 14 m (72 layers);
	mean: 2 m, min: 0.1 m, max: 5 m 41 layers)		mean: 4.9 m, min: 1.1 m, max: 14 m (90 layers);
			mean: 4.1 m, min: 1.1 m, max: 14 m (120 layers)
$\nu_{C,\text{stab}}$	1×10^{-3} m^2 s^{-1}	1×10^{-3} m^2 s^{-1}	1×10^{-3} m^2 s^{-1}
$\kappa_{C,\text{stab}}$	5×10^{-5} m^2 s^{-1}	5×10^{-5} m^2 s^{-1}	5×10^{-5} m^2 s^{-1}
$\nu_{C,\text{unstab}}$	0.1 m^2 s^{-1}	0.1 m^2 s^{-1}	0.1 m^2 s^{-1}
$\kappa_{C,\text{unstab}}$	0.1 m^2 s^{-1}	0.1 m^2 s^{-1}	0.1 m^2 s^{-1}
FMT details	Fluxes distributed into top cell	Fluxes distributed into top cell for COM config); and, over prescribed depth (2 m to 40 m) for other configurations, with equal distribution with depth	Fluxes distributed over prescribed depth; Decreasing exponential distribution with depth
TSD details	Tracers sampled from top grid cells	Tracers sampled from top grid cells	Tracers averaged over fixed depth
u* sampling distance	Velocities averaged from the u-/v-points (cell edges) to the top model layer rho-points (center of each cell)	Velocity at the tracer point (center of each cell) estimated from the velocity points (vertices)	Normal velocities at edges in the top model layer used to reconstruct velocity magnitude and u_* at cell centres
Momentum BC	Quadratic drag law	Quadratic drag law	Quadratic drag law
C_D	2.5×10^{-3}	2.5×10^{-3}	2.5×10^{-3}

number of vertical layers in the model as well as with depth and horizontal coordinate. To give the reader a flavor for typical values, in Supplementary Table A.1, we provide the mean, minimum and maximum thickness of the top model layer under the ice shelf for various numbers of vertical layers.

Heat and salt fluxes are distributed exponentially with depth with a vertical length scale given by FMT (ζ), so that the flux into layer k with layer thickness h_k is

$$Q_1 = Q_{\text{surf}} \left(1 - e^{-h_1/\zeta}\right), \tag{A.2}$$

$$R_1 = Q_{\text{surf}} - Q_1, \tag{A.3}$$

$$Q_k = R_{k-1} \left(1 - e^{-h_k/\zeta}\right), \tag{A.4}$$

$$R_k = R_{k-1} - Q_k, \tag{A.5}$$

where Q_{surf} is the total surface flux, Q_k is the flux into layer k and R_k is a 'residual' flux at the bottom of layer k that is available for distribution into lower layers. This scheme is *not* used for momentum fluxes.

The 'far-field' tracer values used in the 3-equation boundary conditions (Eqs. (1)–(3)) are computed by a simple weighted average over the TSD (h_{TS}):

$$T_w = \frac{\left(\sum_{k=1}^{k'-1} h_k T_k\right) + h'_{k'} T_{k'}}{h_{\text{TS}}}, \tag{A.6}$$

$$h'_{k'} = h_{\text{TS}} - \sum_{k=1}^{k'-1} h_k, \tag{A.7}$$

and similarly for S_w, where k' is the index of the deepest layer with a top interface that is within a distance h_{TS} of the ice-shelf base.

References

Adcroft, A., Campin, J.-M., 2004. Rescaled height coordinates for accurate representation of free-surface flows in ocean circulation models. Ocean Model. 7 (3), 269–284. http://dx.doi.org/10.1016/j.ocemod.2003.09.003.

Adcroft, A., Hill, C., Marshall, J., 1997. Representation of topography by shaved cells in a height coordinate ocean model. Mon. Weather Rev. 125 (9), 2293–2315. http://dx.doi.org/10.1175/1520-0493(1997)125<2293:ROTBSC>2.0.CO;2.

Arrigo, K.R., van Dijken, G.L., Strong, A.L., 2015. Environmental controls of marine productivity hot spots around Antarctica. J. Geophys. Res.: Oceans 120 (8), 5545–5565. http://dx.doi.org/10.1002/2015JC010888.

Asay-Davis, X.S., Cornford, S.L., Durand, G., Galton-Fenzi, B.K., Gladstone, R.M., Gudmundsson, G.H., Hattermann, T., Holland, D.M., Holland, D., Holland, P.R., et al., 2016. Experimental design for three interrelated marine ice sheet and ocean model intercomparison projects: MISMIP v. 3 (MISMIP+), ISOMIP v. 2 (ISOMIP+) and MISOMIP v. 1 (MISOMIP1). Geosci. Model Dev. 9 (7), 2471–2497.

Bushuk, M., Holland, D.M., Stanton, T.P., Stern, A., Gray, C., 2019. Ice scallops: a laboratory investigation of the ice–water interface. J. Fluid Mech. 873, 942–976. http://dx.doi.org/10.1017/jfm.2019.398.

Church, J.A., Clark, P.U., Cazenave, A., Gregory, J.M., Jevrejeva, S., Levermann, A., Merrifield, M.A., Milne, G.A., Nerem, R.S., Nunn, P.D., Payne, A.J., Pfeffer, W.T., Stammer, D., Unnikrishnan, A.S., 2013. Sea level change. In: Stocker, T., Qin, D., Plattner, G.-K., Tignor, M., Allen, S., Boschung, J., Nauels, A., Xia, Y., Bex, V., Midgley, P. (Eds.), Climate Change 2013: The Physical Science Basis. Contribution of Working Group I to the Fifth Assessment Report of the Intergovernmental Panel on Climate Change. Cambridge University Press, Cambridge, United Kingdom, New York, NY, USA, pp. 1137–1216.

Dansereau, V., Heimbach, P., Losch, M., 2014. Simulation of subice shelf melt rates in a general circulation model: Velocity-dependent transfer and the role of friction. J. Geophys. Res.: Oceans 119 (3), 1765–1790. http://dx.doi.org/10.1002/2013JC008846.

Davis, P.E., Nicholls, K.W., 2019. Turbulence observations beneath larsen C ice shelf, Antarctica. J. Geophys. Res.: Oceans 124 (8), 5529–5550. http://dx.doi.org/10.1029/2019jc015164.

DeConto, R.M., Pollard, D., 2016. Contribution of Antarctica to past and future sea-level rise. Nature 531 (7596), 591–597. http://dx.doi.org/10.1038/nature17145.

Dinniman, M., Asay-Davis, X., Galton-Fenzi, B., Holland, P., Jenkins, A., Timmermann, R., 2016. Modeling ice shelf/ocean interaction in Antarctica: A review. Oceanography 29 (4), 144–153. http://dx.doi.org/10.5670/oceanog.2016.106.

Dinniman, M.S., Klinck, J.M., Bai, L.-S., Bromwich, D.H., Hines, K.M., Holland, D.M., 2015. The effect of atmospheric forcing resolution on delivery of ocean heat to the Antarctic floating ice shelves*,+. J. Clim. 28 (15), 6067–6085.

Dinniman, M.S., Klinck, J.M., Smith, W.O., 2007. Influence of sea ice cover and icebergs on circulation and water mass formation in a numerical circulation model of the Ross Sea, Antarctica. J. Geophys. Res. 112 (C11), C11013. http://dx.doi.org/10.1029/2006JC004036.

Ezer, T., Mellor, G.L., 2004. A generalized coordinate ocean model and a comparison of the bottom boundary layer dynamics in terrain-following and in z-level grids. Ocean Model. 6 (3), 379–403. http://dx.doi.org/10.1016/S1463-5003(03)00026-X.

Galton-Fenzi, B.K., 2009. Modelling Ice-Shelf/Ocean Interaction (Ph.D. thesis). University of Tasmania, pp. 1–165.

Galton-Fenzi, B.K., Hunter, J.R., Coleman, R., Marsland, S.J., Warner, R.C., 2012. Modeling the basal melting and marine ice accretion of the Amery Ice Shelf. J. Geophys. Res. 117 (C9), C09031. http://dx.doi.org/10.1029/2012JC008214.

Gayen, B., Griffiths, R.W., Kerr, R.C., 2016. Simulation of convection at a vertical ice face dissolving into saline water. J. Fluid Mech. 798, 284–298. http://dx.doi.org/10.1017/jfm.2016.315.

Goldberg, D.N., Little, C.M., Sergienko, O.V., Gnanadesikan, A., Hallberg, R., Oppenheimer, M., 2012a. Investigation of land ice-ocean interaction with a fully coupled ice-ocean model: 1. Model description and behavior. J. Geophys. Res. 117 (F2), F02037. http://dx.doi.org/10.1029/2011JF002246.

Goldberg, D.N., Little, C.M., Sergienko, O.V., Gnanadesikan, A., Hallberg, R., Oppenheimer, M., 2012b. Investigation of land ice-ocean interaction with a fully coupled ice-ocean model: 2. Sensitivity to external forcings. J. Geophys. Res. 117 (F2), F02038. http://dx.doi.org/10.1029/2011JF002247.

Grosfeld, K., Gerdes, R., Determann, J., 1997. Thermohaline circulation and interaction between ice shelf cavities and the adjacent open ocean. J. Geophys. Res. 102 (C7), 15595. http://dx.doi.org/10.1029/97JC00891.

Gwyther, D.E., Cougnon, E.A., Galton-Fenzi, B.K., Roberts, J.L., Hunter, J.R., Dinniman, M.S., 2016. Modelling the response of ice shelf basal melting to different ocean cavity environmental regimes. Ann. Glaciol. 57 (73), 131–141. http://dx.doi.org/10.1017/aog.2016.31.

Gwyther, D.E., Galton-Fenzi, B.K., Dinniman, M.S., Roberts, J.L., Hunter, J.R., 2015. The effect of basal friction on melting and freezing in ice shelf-ocean models. Ocean Model. 95, 38–52. http://dx.doi.org/10.1016/j.ocemod.2015.09.004.

Gwyther, D.E., Galton-Fenzi, B.K., Hunter, J.R., Roberts, J.L., 2014. Simulated melt rates for the Totten and Dalton ice shelves. Ocean Sci. 10 (3), 267–279. http://dx.doi.org/10.5194/os-10-267-2014.

Haney, R.L., 1991. On the pressure gradient force over steep topography in sigma coordinate ocean models. J. Phys. Oceanogr. 21 (4), 610–619. http://dx.doi.org/10.1175/1520-0485(1991)021<0610:OTPGFO>2.0.CO;2.

Hellmer, H.H., Olbers, D.J., 1989. A two-dimensional model for the thermohaline circulation under an ice shelf. Antarct. Sci. 1 (4), 325–336.

Holland, D.M., Jenkins, A., 1999. Modeling thermodynamic ice-ocean interactions at the base of an ice shelf. J. Phys. Oceanogr. 29 (8), 1787–1800. http://dx.doi.org/10.1175/1520-0485(1999)029<1787:MTIOIA>2.0.CO;2.

Holland, D.M., Jenkins, A., 2001. Adaptation of an isopycnic coordinate ocean model for the study of circulation beneath ice shelves. Mon. Weather Rev. 129 (8), 1905–1927. http://dx.doi.org/10.1175/1520-0493(2001)129<1905:AOAICO>2.0.CO;2.

Holland, P.R., Jenkins, A., Holland, D.M., 2008. The response of ice shelf basal melting to variations in ocean temperature. J. Clim. 21 (11), 2558–2572. http://dx.doi.org/10.1175/2007JCLI1909.1.

Hunter, J.R., 2006. Specification for Test Models of Ice Shelf Cavities. Technical Report June, Antarctic Climate & Ecosystems Cooperative Research Centre, pp. 1–17.

Jacobs, S.S., Giulivi, C.F., 2010. Large multidecadal salinity trends near the Pacific–Antarctic continental margin. J. Clim. 23 (17), 4508–4524. http://dx.doi.org/10.1175/2010JCLI3284.1.

Jenkins, A., 2016. A simple model of the ice shelf–ocean boundary layer and current. J. Phys. Oceanogr. 46 (6), 1785–1803. http://dx.doi.org/10.1175/JPO-D-15-0194.1.

Jenkins, A., Nicholls, K.W., Corr, H.F.J., 2010. Observation and parameterization of ablation at the base of Ronne Ice Shelf, Antarctica. J. Phys. Oceanogr. 40 (10), 2298–2312. http://dx.doi.org/10.1175/2010JPO4317.1.

Kader, B.A., Yaglom, A.M., 1972. Heat and mass transfer laws for fully turbulent wall flows. Int. J. Heat Mass Transfer 15 (12), 2329–2351. http://dx.doi.org/10.1016/0017-9310(72)90131-7.

Kimura, S., Candy, A.S., Holland, P.R., Piggott, M.D., Jenkins, A., 2013. Adaptation of an unstructured-mesh, finite-element ocean model to the simulation of ocean circulation beneath ice shelves. Ocean Model. 67, 39–51. http://dx.doi.org/10.1016/j.ocemod.2013.03.004.

Kimura, S., Nicholls, K.W., Venables, E., 2015. Estimation of ice shelf melt rate in the presence of a thermohaline staircase. J. Phys. Oceanogr. 45 (1), 133–148. http://dx.doi.org/10.1175/JPO-D-14-0106.1.

Kusahara, K., Hasumi, H., 2013. Modeling Antarctic ice shelf responses to future climate changes and impacts on the ocean. J. Geophys. Res.: Oceans 118 (5), 2454–2475. http://dx.doi.org/10.1002/jgrc.20166.

Kusahara, K., Hasumi, H., 2014. Pathways of basal meltwater from Antarctic ice shelves: A model study. J. Geophys. Res.: Oceans 119, 2227–2237. http://dx.doi.org/10.1002/2013JC009305.Received.

Kusahara, K., Hasumi, H., Fraser, A.D., Aoki, S., Shimada, K., Williams, G.D., Massom, R., Tamura, T., 2017. Modeling ocean–cryosphere interactions off Adélie and George V Land, East Antarctica. J. Clim. 30 (1), 163–188.

Large, W.G., McWilliams, J.C., Doney, S.C., 1994. Oceanic vertical mixing: A review and a model with a nonlocal boundary layer parameterization. Rev. Geophys. 32 (4), 363. http://dx.doi.org/10.1029/94RG01872.

Little, C.M., Gnanadesikan, A., Hallberg, R., 2008. Large-scale oceanographic constraints on the distribution of melting and freezing under ice shelves. J. Phys. Oceanogr. 38 (10), 2242–2255. http://dx.doi.org/10.1175/2008JPO3928.1.

Little, C.M., Gnanadesikan, A., Oppenheimer, M., 2009. How ice shelf morphology controls basal melting. J. Geophys. Res.: Oceans 114 (12), C12007. http://dx.doi.org/10.1029/2008JC005197.

Liu, Y., Moore, J.C., Cheng, X., Gladstone, R.M., Bassis, J.N., Liu, H., Wen, J., Hui, F., 2015. Ocean-driven thinning enhances iceberg calving and retreat of Antarctic ice shelves. Proc. Natl. Acad. Sci. 112 (11), 3263–3268. http://dx.doi.org/10.1073/pnas.1415137112.

Losch, M., 2008. Modeling ice shelf cavities in a z coordinate ocean general circulation model. J. Geophys. Res.: Oceans 113, C08043. http://dx.doi.org/10.1029/2007JC004368.

Magorrian, S.J., Wells, A.J., 2016. Turbulent plumes from a glacier terminus melting in a stratified ocean. J. Geophys. Res.: Oceans 121 (7), 4670–4696. http://dx.doi.org/10.1002/2015JC011160.

Mathiot, P., Jenkins, A., Harris, C., Madec, G., 2017. Explicit representation and parametrised impacts of under ice shelf seas in the z* coordinate ocean model NEMO 3.6. Geosci. Model Dev. 10 (7), 2849–2874. http://dx.doi.org/10.5194/gmd-10-2849-2017.

McConnochie, C.D., Kerr, R.C., 2017. Testing a common ice-ocean parameterization with laboratory experiments. J. Geophys. Res.: Oceans 122 (7), 5905–5915. http://dx.doi.org/10.1002/2017JC012918.

McConnochie, C.D., Kerr, R.C., 2018. Dissolution of a sloping solid surface by turbulent compositional convection. J. Fluid Mech. 846, 563–577. http://dx.doi.org/10.1017/jfm.2018.282.

McPhee, M., 1992. Turbulent heat flux in the upper ocean under sea ice. J. Geophys. Res. 97, 5365–5379.

McPhee, M., Kottmeier, C., 1999. Ocean heat flux in the central Weddell Sea during winter. J. Phys. Oceanogr. 29 (6), 1166–1179. http://dx.doi.org/10.1175/1520-0485(1999)029<1166:OHFITC>2.0.CO;2.

McPhee, M.G., Maykut, G.A., Morison, J.H., 1987. Dynamics and thermodynamics of the ice/upper ocean system in the marginal ice zone of the Greenland Sea. J. Geophys. Res. 92, 7017–7031. http://dx.doi.org/10.1029/JC092iC07p07017.

Mondal, M., Gayen, B., Griffiths, R.W., Kerr, R.C., 2019. Ablation of sloping ice faces into polar seawater. J. Fluid Mech. 863, 545–571. http://dx.doi.org/10.1017/jfm.2018.970.

Petersen, M., Jacobsen, D.W., Ringler, T.D., Hecht, M.W., Maltrud, M.E., 2014. Evaluation of the arbitrary Langrangian–Eulerian vertical coordinate method in the MPAS-Ocean model. Ocean Model. http://dx.doi.org/10.1016/j.ocemod.2014.12.004.

Rees Jones, D.W., Wells, A.J., 2018. Frazil-ice growth rate and dynamics in mixed layers and sub-ice-shelf plumes. Cryosphere 12 (1), 25–38. http://dx.doi.org/10.5194/tc-12-25-2018.

Ringler, T., Petersen, M., Higdon, R.L., Jacobsen, D., Jones, P.W., Maltrud, M., 2013. A multi-resolution approach to global ocean modeling. Ocean Model. 69, 211–232. http://dx.doi.org/10.1016/j.ocemod.2013.04.010.

Robinson, N.J., Stevens, C.L., McPhee, M.G., 2017. Observations of amplified roughness from crystal accretion in the sub-ice ocean boundary layer. Geophys. Res. Lett. 44 (4), 1814–1822. http://dx.doi.org/10.1002/2016GL071491.

Robinson, N.J., Williams, M.J.M., Barrett, P.J., Pyne, a.R., 2010. Observations of flow and ice-ocean interaction beneath the McMurdo Ice Shelf, Antarctica. J. Geophys. Res.: Oceans 115, C03025. http://dx.doi.org/10.1029/2008JC005255.

Robinson, N.J., Williams, M.J.M., Stevens, C.L., Langhorne, P.J., Haskell, T.G., 2014. Evolution of a supercooled Ice Shelf Water plume with an actively growing subice platelet matrix. J. Geophys. Res.: Oceans 119 (6), 3425–3446. http://dx.doi.org/10.1002/2013JC009399.

Schodlok, M., Menemenlis, D., Rignot, E., 2016. Ice shelf basal melt rates around Antarctica from simulations and observations. J. Geophys. Res.: Oceans 121 (2), 1085–1109.

Schoof, C., 2007. Ice sheet grounding line dynamics: Steady states, stability, and hysteresis. J. Geophys. Res. 112 (F3), F03S28. http://dx.doi.org/10.1029/2006JF000664.

Shchepetkin, A.F., McWilliams, J.C., 2003. A method for computing horizontal pressure-gradient force in an oceanic model with a nonaligned vertical coordinate. J. Geophys. Res. 108 (C3), 1–34. http://dx.doi.org/10.1029/2001JC001047.

Shchepetkin, A.F., McWilliams, J.C., 2005. The regional oceanic modeling system (ROMS): a split-explicit, free-surface, topography-following-coordinate oceanic model. Ocean Model. 9 (4), 347–404. http://dx.doi.org/10.1016/j.ocemod.2004.08.002.

Shepherd, A., Gilbert, L., Muir, A.S., Konrad, H., McMillan, M., Slater, T., Briggs, K.H., Sundal, A.V., Hogg, A.E., Engdahl, M.E., 2019. Trends in Antarctic ice sheet elevation and mass. Geophys. Res. Lett. 46 (14), 8174–8183. http://dx.doi.org/10.1029/2019gl082182.

Shepherd, A., Ivins, E., Rignot, E., Smith, B., Van Den Broeke, M., Velicogna, I., Whitehouse, P., Briggs, K., Joughin, I., Krinner, G., Nowicki, S., Payne, T., Scambos, T., Schlegel, N., Geruo, A., Agosta, C., Ahlstrøm, A., Babonis, G., Barletta, V., Blazquez, A., Bonin, J., Csatho, B., Cullather, R., Felikson, D., Fettweis, X., Forsberg, R., Gallee, H., Gardner, A., Gilbert, L., Groh, A., Gunter, B., Hanna, E., Harig, C., Helm, V., Horvath, A., Horwath, M., Khan, S., Kjeldsen, K.K., Konrad, H., Langen, P., Lecavalier, B., Loomis, B., Luthcke, S., McMillan, M., Melini, D., Mernild, S., Mohajerani, Y., Moore, P., Mouginot, J., Moyano, G., Muir, A., Nagler, T., Nield, G., Nilsson, J., Noel, B., Otosaka, I., Pattle, M.E., Peltier, W.R., Pie, N., Rietbroek, R., Rott, H., Sandberg-Sørensen, L., Sasgen, I., Save, H., Scheuchl, B., Schrama, E., Schröder, L., Seo, K.W., Simonsen, S., Slater, T., Spada, G., Sutterley, T., Talpe, M., Tarasov, L., Van De Berg, W.J., Van Der Wal, W., Van Wessem, M., Vishwakarma, B.D., Wiese, D., Wouters, B., 2018. Mass balance of the Antarctic ice sheet from 1992 to 2017. Nature 558 (7709), 219–222. http://dx.doi.org/10.1038/s41586-018-0179-y.

Soulsby, R.L., 1983. The bottom boundary layer of shelf seas. In: Johns, B. (Ed.), Physical Oceanography of Coastal and Shelf Seas. Elsevier Science Publishers B.V., Amsterdam, pp. 189–266.

Stanton, T.P., Shaw, W.J., Truffer, M., Corr, H.F.J., Peters, L.E., Riverman, K.L., Bindschadler, R., Holland, D.M., Anandakrishnan, S., 2013. Channelized ice melting in the ocean boundary layer beneath Pine Island Glacier, Antarctica. Science 341 (6151), 1236–1239. http://dx.doi.org/10.1126/science.1239373.

Stewart, C.L., 2017. Ice-ocean interactions beneath the north-western Ross Ice Shelf, Antarctica. (Ph.D. thesis). University of Cambridge, pp. 1–220.

Timmermann, R., Wang, Q., Hellmer, H.H., 2012. Ice-shelf basal melting in a global finite-element sea-ice/ice-shelf/ocean model. Ann. Glaciol. 53 (60), 303–314. http://dx.doi.org/10.3189/2012AoG60A156.

Vreugdenhil, C.A., Taylor, J.R., 2019. Stratification effects in the turbulent boundary layer beneath a melting ice shelf: insights from resolved large-eddy simulations. J. Phys. Oceanogr. http://dx.doi.org/10.1175/JPO-D-18-0252.1.

Weertman, J., 1974. Stability of the junction of an ice sheet and an ice shelf. J. Glaciol. 13 (67), 3–11.

Zhou, Q., Hattermann, T., 2020. Modeling ice shelf cavities in the unstructured-grid, Finite Volume Community Ocean Model: Implementation and effects of resolving small-scale topography. Ocean Model. 146, 101536. http://dx.doi.org/10.1016/j.ocemod.2019.101536.